

RESEARCH ARTICLE

10.1002/2014JB011607

Key Points:

- Virtual seismograms are constructed by source-receiver interferometry (SRI)
- Ambient noise interferometry constructs robust SRI propagators over 1500 km
- Correlation-convolution SRI constructs seismograms even in attenuative media

Correspondence to:

E. Entwistle,
E.Entwistle@ed.ac.uk

Citation:

Entwistle, E., A. Curtis, E. Galetti, B. Baptie, and G. Meles (2015), Constructing new seismograms from old earthquakes: Retrospective seismology at multiple length scales, *J. Geophys. Res. Solid Earth*, 120, 2466–2490, doi:10.1002/2014JB011607.

Received 16 SEP 2014

Accepted 15 FEB 2015

Accepted article online 20 FEB 2015

Published online 13 APR 2015

Constructing new seismograms from old earthquakes: Retrospective seismology at multiple length scales

Elizabeth Entwistle¹, Andrew Curtis¹, Erica Galetti¹, Brian Baptie², and Giovanni Meles¹

¹School of GeoSciences, University of Edinburgh, Edinburgh, UK, ²British Geological Survey, Edinburgh, UK

Abstract If energy emitted by a seismic source such as an earthquake is recorded on a suitable backbone array of seismometers, source-receiver interferometry (SRI) is a method that allows those recordings to be projected to the location of another target seismometer, providing an estimate of the seismogram that would have been recorded at that location. Since the other seismometer may not have been deployed at the time at which the source occurred, this renders possible the concept of “retrospective seismology” whereby the installation of a sensor at one period of time allows the construction of virtual seismograms as though that sensor had been active before or after its period of installation. Here we construct such virtual seismograms on target sensors in both industrial seismic and earthquake seismology settings, using both active seismic sources and ambient seismic noise to construct SRI *propagators*, and on length scales ranging over 5 orders of magnitude from ~40 m to ~2500 km. In each case we compare seismograms constructed at target sensors by SRI to those actually recorded on the same sensors. We show that spatial integrations required by interferometric theory can be calculated over irregular receiver arrays by embedding these arrays within 2-D spatial Voronoi cells, thus improving spatial interpolation and interferometric results. The results of SRI are significantly improved by restricting the backbone receiver array to include approximately those receivers that provide a stationary-phase contribution to the interferometric integrals. Finally, we apply both correlation-correlation and correlation-convolution SRI and show that the latter constructs fewer nonphysical arrivals.

1. Introduction

Traditional seismology uses the propagation of elastic waves from large earthquakes or explosions to infer earthquake or Earth properties and structure. This encouraged the deployment of seismometer networks worldwide, particularly in regions of high seismicity. However, earthquake seismogram data are only sensitive to earth properties on paths of energy propagation between earthquakes and seismometers. Recent developments in the field of seismic or wavefield interferometry (sometimes referred to as Green's function retrieval) create new data types that are sensitive to a variety of different spatial volumes using the same seismometer networks and seismic source distributions (for reviews, see Curtis *et al.* [2006], Wapenaar *et al.* [2010a, 2010b], and Galetti and Curtis [2012]). Here we investigate a new such method, on a range of spatial and temporal scales.

Seismic interferometry refers broadly to processes of cross-correlation, convolution, or deconvolution that estimate the Green's function between two receivers (inter-receiver interferometry), two sources (inter-source interferometry), or a source and a receiver (source-receiver interferometry). Inter-receiver interferometry [Weaver and Lobkis, 2001; Campillo and Paul, 2003; Wapenaar, 2003, 2004; van Manen *et al.*, 2005, 2006; Wapenaar and Fokkema, 2006] allows one to construct the seismic signals that would have been recorded at one receiver location if an energy source had been fired at the location of the other receiver (the so-called “virtual source” location), while inter-source interferometry [Hong and Menke, 2006; Curtis *et al.*, 2009; Tonegawa and Nishida, 2010; Poliannikov *et al.*, 2012] allows one to construct the response from one of the sources that would have been recorded at the location of the other source (i.e., as if a “virtual receiver” had been active at the location of the other source). Since their inception, these methods have been widely used in exploration seismics (e.g., Schuster [2001]; Schuster *et al.* [2004]; Bakulin and Calvert [2004]; Xiao *et al.* [2006]; Halliday *et al.* [2007, 2010, 2012]; Draganov *et al.* [2013]) and regional seismology (e.g., Shapiro and Campillo [2004]; Roux *et al.* [2005]; Sabra *et al.* [2005a, 2005b]; Shapiro *et al.* [2005]; Stehly *et al.* [2007, 2008]; Wang *et al.* [2008]; Bensen *et al.* [2008]; Curtis *et al.* [2009]; Nicolson *et al.* [2012]). They have also been significantly advanced and tested in a number of other fields, including acoustics and ultrasonics [Cassereau

and Fink, 1993; Roux and Fink, 2003; Weaver and Lobkis, 2001; Derode et al., 2003a, 2003b), helioseismology [Rickett and Claerbout, 1999], structural engineering [Snieder and Safak, 2006], medical diagnostics [Sabra et al., 2007], and electromagnetics [Slob et al., 2007; Slob and Wapenaar, 2007].

Source-receiver interferometry (SRI) is a third form that acts rather differently from inter-receiver and inter-source interferometry. It can be derived either directly from representation theorems [Curtis and Halliday, 2010; Halliday and Curtis, 2010] or by combining the theories of inter-receiver and inter-source interferometry [Curtis, 2009; Curtis et al., 2012]. The result is that a Green's function between a source and a receiver can be estimated from seismograms recorded on an array of other receivers (herein referred to as a backbone array) from a set of other sources. This has led to the development of new algorithms for imaging [Halliday and Curtis, 2010; Vasconcelos et al., 2010; Poliannikov, 2011; Poliannikov et al., 2012; Vasconcelos and Rickett, 2013; Ravasi and Curtis, 2013a, 2013b; Vasconcelos, 2013; Ravasi et al., 2014], noise removal [Duguid et al., 2011], methods to correct for errors in inter-receiver and inter-source interferometry [King and Curtis, 2012; Meles and Curtis, 2014a], and methods to analyze and synthesize scattered wavefields (e.g., L er et al. [2014a]; Meles and Curtis [2014b]; L er et al. [2014b]). All of these methods involve using SRI for some form of spatial redatuming of recorded data.

Curtis et al. [2012] showed that SRI can also be used for a type of temporal redatuming: using recordings of earthquake sources made on a backbone seismometer array, virtual seismograms of the same source events can be constructed on receivers that were not deployed at the time of the event. Thus, a form of "retrospective" seismology is possible whereby one reconstructs the signals from an energy source at the location of a new seismometer, chosen retrospectively after that source occurred and after all energy from it has dissipated. One can thus use the benefit of hindsight of the source location and magnitude estimates to decide at which new locations to construct new (virtual) seismograms from that source.

This method may have significant implications within earthquake seismology: in the days following a large earthquake, temporary seismometers might be deployed closer to the earthquake epicentre to measure subsequent seismic activity in the area. Using a backbone array of seismometers that did record the earthquake energy, in principle one can spatially and temporally redatum the energy fluctuations from the main event onto the set of temporary seismometers. Curtis et al. [2012] demonstrated this idea by reconstructing seismic signals from two earthquakes in New Zealand on a set of temporary seismometers, some of which were not actively recording data when the earthquakes occurred. The new seismograms obtained were used to estimate seismic velocities in the vicinity of the seismometers, and theory was presented that allows information about the source phase to be obtained from such virtual seismograms.

There are parallels between this method and the virtual earthquake approach of Denolle et al. [2013]. The latter authors use traditional inter-receiver interferometry and ambient noise to construct far-field surface wave seismograms that can be directly compared with real earthquake observations: surface impulse responses are constructed using the ambient seismic noise field and are then modified to correct for both depth and the double-couple focal mechanism of an earthquake [Denolle et al., 2013, 2014]. This turns one of the receivers in the pair into a virtual earthquake source. To test this method, however, one requires a real earthquake source and a seismometer to be located close to the virtual source location. In contrast, SRI theory places no such constraints on the locations of source and receiver pairs.

In this paper we test and extend the SRI method by reconstructing virtual seismograms (of both active seismic shots and earthquakes) with varying degrees of accuracy over a range of inter-receiver length scales spanning 5 orders of magnitude—from approximately 40 m to 2500 km. Each length scale is determined by the distance between a new "target" sensor and a backbone array of receivers that recorded the source energy. In one example, we directly compare correlational and convolutional methods for SRI at the same sensors. We also use correlation-convolution SRI to extend the target sensor geometry, thus reaching length scales of up to 2420 km which allows the limitations of the SRI method to be assessed. At this largest length scale we show that the spatial extent of the backbone array significantly affects the accuracy of numerical approximations of interferometric integrals, and thus of SRI seismograms: longer arrays are not necessarily better.

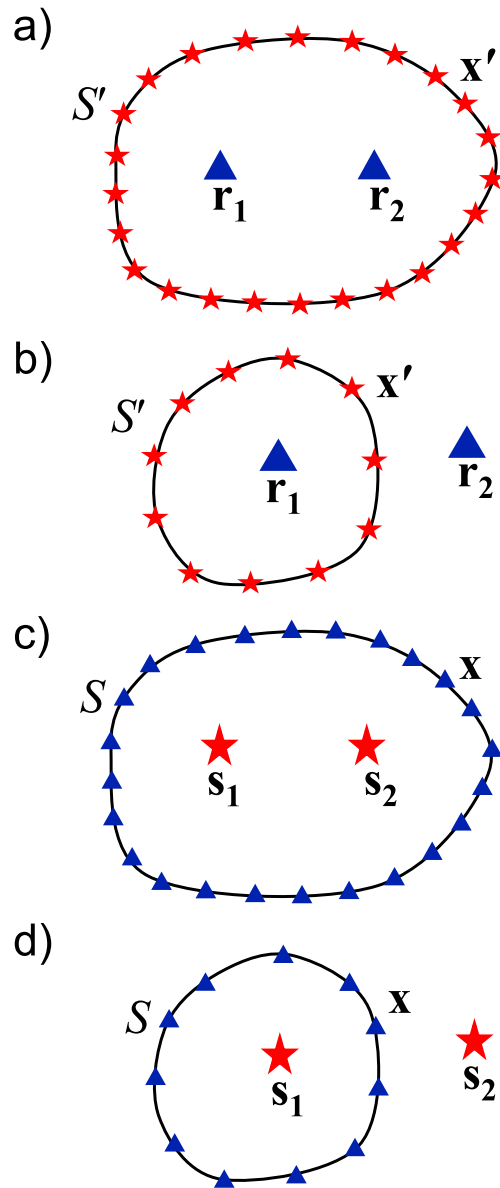


Figure 1. Schematic source and receiver geometries for (a and b) inter-receiver interferometry and (c and d) inter-source interferometry to construct the Green's function $G(\mathbf{r}_1, \mathbf{r}_2)$ or $G(\mathbf{s}_1, \mathbf{s}_2)$. Stars are sources, triangles are receivers. In Figures 1a and 1b the responses from each source at locations \mathbf{x}' on boundary S' are recorded on receivers \mathbf{r}_1 and \mathbf{r}_2 which are then (Figure 1a) cross-correlated or (Figure 1b) convolved. (Figures 1c and 1d) By applying source-receiver reciprocity to (Figures 1a) and (1b), the responses from sources at \mathbf{s}_1 and \mathbf{s}_2 are recorded by each receiver at locations \mathbf{x} on boundary S and (Figure 1c) cross-correlated or (Figure 1d) convolved. In all four cases the results of all cross-correlations or convolutions are summed (integrated over S' or S) to obtain an approximation of the Green's function between \mathbf{r}_1 and \mathbf{r}_2 or \mathbf{s}_1 and \mathbf{s}_2 .

component of the normal vector on the boundary S' and ∂_k denotes a spatial derivative in the k direction. $G(\mathbf{r}_1, \mathbf{x}')$ and $\partial_i G(\mathbf{r}_1, \mathbf{x}') n_i$ represent the pressure at \mathbf{r}_1 due to monopole and dipole volume injection rate density sources at \mathbf{x}' on S' , respectively, where the dipole sources are oriented normal to the boundary S' .

2. Method

SRI may be applied in two steps [Curtis et al., 2012]: (1) An inter-receiver interferometry step constructs estimates of the Green's functions between the backbone array seismometers and the target sensors; these Green's functions are called the *propagators* in SRI; and (2) these propagators are used to project the recordings of the source energy on the backbone array to the location of the target sensor. In this section we describe inter-receiver and inter-source interferometry first, then how they are combined in SRI.

Both inter-receiver and inter-source interferometry can be performed using cross correlation [e.g., Campillo and Paul, 2003; Wapenaar, 2003, 2004; van Manen et al., 2005, 2006; Wapenaar and Fokkema, 2006], convolution [e.g., Slob and Wapenaar, 2007; Halliday and Curtis, 2009], or deconvolution [e.g., Snieder and Safak, 2006; Snieder et al., 2006a; Wapenaar et al., 2008; Vasconcelos and Snieder, 2008a, 2008b; Wapenaar et al., 2011]. Here we focus on methods of cross-correlation and convolution but reviews and derivations of all techniques can be found in Curtis et al. [2006], Snieder et al. [2009], Schuster [2009], Wapenaar et al. [2010a, 2010b], and Galetti and Curtis [2012].

2.1. Inter-Receiver Interferometry

Consider the geometry in Figure 1a where two receivers at \mathbf{r}_1 and \mathbf{r}_2 are surrounded by impulsive sources at positions \mathbf{x}' on boundary S' . The responses from sources at \mathbf{x}' are recorded at \mathbf{r}_1 and \mathbf{r}_2 , cross correlated and summed (integrated) over the boundary S' . This constructs an estimate of the Green's function between points \mathbf{r}_1 and \mathbf{r}_2 [Wapenaar and Fokkema, 2006]. The Green's function is the response that would have been recorded at receiver \mathbf{r}_2 if there had been an impulsive source at the location of receiver \mathbf{r}_1 . The receiver at \mathbf{r}_1 is thus turned into a virtual (imagined) source. For waves propagating in an acoustic medium, this process is represented in the frequency domain by the following surface integral [Wapenaar and Fokkema, 2006]:

$$G(\mathbf{r}_2, \mathbf{r}_1) + G^*(\mathbf{r}_2, \mathbf{r}_1) = \int_{S'} \frac{-1}{j\omega\rho(\mathbf{x}')} (G(\mathbf{r}_2, \mathbf{x}') \partial_i G^*(\mathbf{r}_1, \mathbf{x}') - (\partial_i G(\mathbf{r}_2, \mathbf{x}')) G^*(\mathbf{r}_1, \mathbf{x}')) n_i d^2\mathbf{x}' \quad (1)$$

where $j = \sqrt{-1}$, ω is angular frequency, $\rho(\mathbf{x}')$ is the mass density of the medium, n_j is the j th component of the normal vector on the boundary S' and ∂_k denotes a spatial derivative in the k direction.

Boundary S' is arbitrary as long as it encloses \mathbf{r}_1 and \mathbf{r}_2 , and $G(\mathbf{r}_2, \mathbf{r}_1)$ contains direct and (multiply) scattered wave contributions from inhomogeneities inside and outside of S' . Einstein's summation principle for repeated indices applies throughout. $G(\mathbf{r}_2, \mathbf{r}_1) + G^*(\mathbf{r}_2, \mathbf{r}_1)$ is the homogeneous Green's function; in the time domain $G(\mathbf{r}_2, \mathbf{r}_1)$ represents the desired Green's function from \mathbf{r}_1 to \mathbf{r}_2 , while $G^*(\mathbf{r}_2, \mathbf{r}_1)$ represents the complex conjugate of the same Green's function, which in the time domain represents the same Green's function but starting at zero time and extending in the negative time direction. Either positive or negative times of the homogeneous Green's function thus represent the response recorded at \mathbf{r}_2 from an impulsive source at the location of \mathbf{r}_1 . Note that in the frequency domain the definition of cross correlation is the product of one term with the complex conjugate of another, as on the right side of equation (1).

If the boundary S' only surrounds one receiver as in Figure 1b then a similar set of operations are carried out to estimate $G(\mathbf{r}_2, \mathbf{r}_1)$, but instead of using correlation in this case, the boundary source recordings must be convolved [Wapenaar and Fokkema, 2006]:

$$G(\mathbf{r}_2, \mathbf{r}_1) = \int_{S'} \frac{-1}{j\omega\rho(\mathbf{x}')} (G(\mathbf{r}_1, \mathbf{x}') \partial_r G(\mathbf{r}_2, \mathbf{x}') - (\partial_r G(\mathbf{r}_1, \mathbf{x}')) G(\mathbf{r}_2, \mathbf{x}')) n_r d^2\mathbf{x}' \quad (2)$$

where, as in equation (1) terms such as $G(\mathbf{r}_1, \mathbf{x}')$ are the Fourier transforms of causal time domain Green's functions $G(\mathbf{r}_1, \mathbf{x}', t)$.

2.2. Inter-Source Interferometry

The theory for inter-source interferometry is obtained by applying source-receiver reciprocity to equation (1) [Curtis *et al.*, 2009; Tonegawa and Nishida, 2010]. Consider now the geometry in Figure 1c where two impulsive sources \mathbf{s}_1 and \mathbf{s}_2 are surrounded by receivers at locations \mathbf{x} on boundary S . The responses from \mathbf{s}_1 and \mathbf{s}_2 are recorded at each \mathbf{x} , cross correlated and the results summed (integrated) over all \mathbf{x} on boundary S . This constructs an estimate of the Green's function between points \mathbf{s}_1 and \mathbf{s}_2 . This Green's function is the response from an impulsive source at \mathbf{s}_1 that would have been recorded had a receiver been placed at \mathbf{s}_2 . The source at \mathbf{s}_2 is thus used as a virtual receiver. For waves propagating in an acoustic medium, this process is represented in the frequency domain by the following integral [Curtis *et al.*, 2009]:

$$G(\mathbf{s}_2, \mathbf{s}_1) + G^*(\mathbf{s}_2, \mathbf{s}_1) = \int_S \frac{-1}{j\omega\rho(\mathbf{x})} (G^*(\mathbf{x}, \mathbf{s}_2) \partial_i G(\mathbf{x}, \mathbf{s}_1) - (\partial_i G^*(\mathbf{x}, \mathbf{s}_2)) G(\mathbf{x}, \mathbf{s}_1)) n_i d^2\mathbf{x} \quad (3)$$

Similarly to the inter-receiver case, inter-source interferometry also takes a convolutional form when the boundary S only surrounds one source as in Figure 1d:

$$G(\mathbf{s}_2, \mathbf{s}_1) = \int_S \frac{-1}{j\omega\rho(\mathbf{x})} (G(\mathbf{x}, \mathbf{s}_2) \partial_i G(\mathbf{x}, \mathbf{s}_1) - (\partial_i G(\mathbf{x}, \mathbf{s}_2)) G(\mathbf{x}, \mathbf{s}_1)) n_i d^2\mathbf{x} \quad (4)$$

2.3. Source-Receiver Interferometry

The three canonical source-receiver geometries for SRI are shown in Figure 2 [Curtis and Halliday, 2010]. In Figure 2a, a source \mathbf{s} and receiver \mathbf{r} are surrounded by a boundary of receivers \mathbf{x} on S and a boundary of sources \mathbf{x}' on S' . For wave propagation in an acoustic medium we then obtain the exact SRI formula

$$G(\mathbf{r}, \mathbf{s}) + G^*(\mathbf{r}, \mathbf{s}) = \frac{-1}{j\omega\rho} \int_S \left\{ \left[\frac{-1}{j\omega\rho} \int_{S'} \{ G^*(\mathbf{r}, \mathbf{x}') n_r \partial_r G(\mathbf{x}, \mathbf{x}') - n_r \partial_r G^*(\mathbf{r}, \mathbf{x}') G(\mathbf{x}, \mathbf{x}') \} dS' \right] n_i \partial_i G(\mathbf{x}, \mathbf{s}) - n_i \partial_i \left[\frac{-1}{j\omega\rho} \int_{S'} \{ G^*(\mathbf{r}, \mathbf{x}') n_r \partial_r G(\mathbf{x}, \mathbf{x}') - n_r \partial_r G^*(\mathbf{r}, \mathbf{x}') G(\mathbf{x}, \mathbf{x}') \} dS' \right] G(\mathbf{x}, \mathbf{s}) \right\} dS \quad (5)$$

where $G(\mathbf{r}, \mathbf{s})$ is the Green's function in the frequency domain representing the pressure at \mathbf{r} due to a volume injection rate density source at \mathbf{s} . Note that all equations have been presented herein for waves propagating in an acoustic medium, thus ignoring the elastic nature of seismic waves. We also assume that the medium outside of each bounding surface (S and S') is approximately homogeneous and isotropic and that the surface S' is large and spherical [Wapenaar and Fokkema, 2006]. For the equivalent exact SRI equation in elastic media, and those equations pertaining to the other possible source-receiver geometries shown schematically in Figure 2, see Curtis and Halliday [2010].

We now discuss how equation (5) can be modified for practical applications where acoustic (and elastic) assumptions are often violated (e.g., boundaries S and S' are incomplete). Assuming high-frequency wave

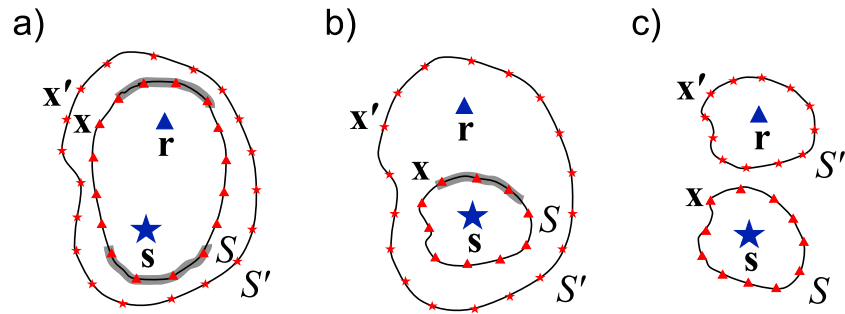


Figure 2. Three possible geometries for source-receiver interferometry (SRI) pertaining to (a) correlation-correlation SRI, (b) correlation-convolution SRI, and (c) convolution-convolution SRI. Key as in Figure 1. The grey-shaded regions in Figures 2a and 2b highlight schematically the stationary-phase regions on the receiver boundary which contribute constructively to energy in SRI integrals; in Figure 2a, only one or other stationary-phase region needs to be used provided that backscattered energy is weak across the boundary. For full derivations of the SRI integrals used in each example, see Curtis and Halliday [2010].

propagation, locally planar wave fronts, and that surfaces S and S' are large and approximately spherical, that the medium outside of the bounding surfaces is homogeneous, and Sommerfeld radiation conditions at the boundary surfaces, Curtis et al. [2012] show that equation (5) can be reduced to two coupled equations:

$$G_H(\mathbf{x}, \mathbf{r}) \cong \frac{2jk}{\omega\rho} \int_{S'} G^*(\mathbf{r}, \mathbf{x}') G(\mathbf{x}, \mathbf{x}') d\mathbf{x}' \quad (6)$$

and

$$G_H(\mathbf{r}, \mathbf{s}) \cong \frac{2jk}{\omega\rho} \int_S G^*(\mathbf{x}, \mathbf{s}) G(\mathbf{x}, \mathbf{r}) d\mathbf{x} \quad (7)$$

Here G_H is the homogeneous Green's function and is defined as $G_H = G + G^*$, where $*$ represents complex conjugation in the frequency domain or time reversal in the time domain. Equation (6) is applied first (step 1 described above) and is simply an approximate representation of inter-receiver interferometry in equation (1) [Wapenaar and Fokkema, 2006]. By isolating only the positive (or negative) times of $G_H(\mathbf{x}, \mathbf{r})$, we identify an estimate of $G(\mathbf{x}, \mathbf{r})$, and doing this for all boundary locations \mathbf{x} we obtain the so-called propagator Green's functions that are used in step 2. Equation (7) then represents the cross correlation of these estimated propagators with the signals recorded from the real source at \mathbf{s} by receivers at all \mathbf{x} on S . This is step 2 above and represents an approximation to inter-source interferometry (equation (3)). In the case represented by Figure 2b, convolution should be used in place of correlation in equation (7):

$$G(\mathbf{r}, \mathbf{s}) \cong \frac{2jk}{\omega\rho} \int_S G(\mathbf{x}, \mathbf{s}) G(\mathbf{x}, \mathbf{r}) d\mathbf{x} \quad (8)$$

Equations (6) and (7) include integrations over all receiver and source positions on boundaries S and S' , respectively. However, Snieder [2004] showed that only a small subset of boundary sources and boundary receivers are required to estimate the Green's function between two points provided that the medium is not too strongly scattering. These sources and receivers lie within regions of the boundaries at which the phase of the integrands in equations (6) and (7) become approximately stationary. Schematic representations of these stationary-phase regions are shown by thick grey lines in Figures 2a and 2b.

Invoking the stationary-phase approximation reduces the number of direct Green's function measurements that need to be made during practical applications of SRI. To reduce this number further, we can replace the active sources at \mathbf{x}' on boundary S' with mutually uncorrelated noise sources [Shapiro and Campillo, 2004; Wapenaar and Fokkema, 2006]. Equation (6) then becomes

$$G_H(\mathbf{x}, \mathbf{r}) \cong C v^*(\mathbf{r}) v(\mathbf{x}) \quad (9)$$

where C is a constant and v is the ambient field fluctuations recorded at \mathbf{x} and \mathbf{r} . When recorded over long periods of time, these ambient field fluctuations may be considered to be a diffusive or random field, and cross correlations of such fields have been found to result in a reasonable estimate of the Green's function

[Lobkis and Weaver, 2001]. Applying equation (9) in place of equation (6) has thus become very attractive in regional seismology as it eliminates the need to measure the response from all sources on a boundary S' individually, and thus, studies no longer need to depend on suitably located earthquakes or other active sources [Shapiro and Campillo, 2004; Shapiro et al., 2005; Sabra et al., 2005a].

In practice, the energy released from an earthquake source has a characteristic source time signature $T(\omega)$. Thus, boundary receivers at locations \mathbf{x} actually record $TG(\mathbf{x}, \mathbf{s})$. Furthermore, T need not be associated with a point source but can be linked to a rupture sequence of point sources over a fault plane F . Recordings R of such rupture sequences on backbone receivers at locations \mathbf{x} can be described approximately by assuming linear additivity of the wavefields from each point source and integrating over all point-source positions \mathbf{s} :

$$R(\mathbf{x}, \bar{\mathbf{s}}) = \int_{\mathbf{s} \in F} T(\mathbf{s})G(\mathbf{x}, \mathbf{s})d\mathbf{s} \quad (10)$$

where $\bar{\mathbf{s}}$ is the set of point sources \mathbf{s} on fault F that represents the earthquake rupture. Our goal in retrospective seismology is thus to estimate

$$R(\mathbf{r}, \bar{\mathbf{s}}) = \int_{\mathbf{s} \in F} T(\mathbf{s})G(\mathbf{r}, \mathbf{s})d\mathbf{s} \quad (11)$$

where \mathbf{r} represents the location of a target sensor that did not necessarily record the seismic energy from the earthquake. If we premultiply equation (7) by $T^*(\mathbf{s})$, integrate over point-sources \mathbf{s} on fault plane F , and apply source-receiver reciprocity, we obtain

$$\begin{aligned} \int_{\mathbf{s} \in F} T(\mathbf{s})^* G_H(\mathbf{r}, \mathbf{s})d\mathbf{s} &\cong \frac{2jk}{\omega\rho} \int_S \int_{\mathbf{s} \in F} [T(\mathbf{s})G(\mathbf{x}, \mathbf{s})]^* G(\mathbf{x}, \mathbf{r})d\mathbf{s}d\mathbf{x} \\ &\cong \frac{2jk}{\omega\rho} \int_S R^*(\mathbf{x}, \bar{\mathbf{s}})G(\mathbf{x}, \mathbf{r})d\mathbf{x} \end{aligned} \quad (12)$$

This shows that if we calculate the right side of equation (12) by cross correlating the propagators $G(\mathbf{x}, \mathbf{r})$ with the event recordings $R(\mathbf{x}, \bar{\mathbf{s}})$ on the backbone array at location \mathbf{x} , integrate over the backbone array, and apply source-receiver reciprocity, we obtain the integral of $T(\mathbf{s})^* G_H(\mathbf{r}, \mathbf{s}) = T(\mathbf{s})^* G(\mathbf{r}, \mathbf{s}) + T(\mathbf{s})^* G^*(\mathbf{r}, \mathbf{s})$ over the fault plane F (left side of equation (12)). At positive times we therefore obtain the integral of $T(\mathbf{s})^* G(\mathbf{r}, \mathbf{s})$: this is not the true response of an earthquake point source \mathbf{s} at receiver \mathbf{r} as G is convolved with the time reverse of the source time signature T rather than with T itself as required by equation (11). However, at negative times we obtain the integral of $T(\mathbf{s})^* G^*(\mathbf{r}, \mathbf{s})$: after time reversal (complex conjugation), this gives the desired $T(\mathbf{s})G(\mathbf{r}, \mathbf{s})$ integrated over fault plane F or $R(\mathbf{r}, \bar{\mathbf{s}})$ in equation (11). Thus, when using correlation-correlation SRI, we use only the acausal part of reconstructed signals to approximate the seismogram responses from earthquake sources at target seismometers \mathbf{r} . Nevertheless, we will discuss the geometry necessary to construct both the causal and acausal sides of the homogeneous Green's function, and the benefits of such a geometry, in section 5 below.

A similar analysis for correlation-convolution SRI in equation (8) shows that the correct seismogram is created by evaluating

$$\begin{aligned} \int_{\mathbf{s} \in F} T(\mathbf{s})G(\mathbf{r}, \mathbf{s})d\mathbf{s} &\cong \frac{2jk}{\omega\rho} \int_S \int_{\mathbf{s} \in F} T(\mathbf{s})G(\mathbf{x}, \mathbf{s})G(\mathbf{x}, \mathbf{r})d\mathbf{s}d\mathbf{x} \\ &\cong \frac{2jk}{\omega\rho} \int_S R(\mathbf{x}, \bar{\mathbf{s}})G(\mathbf{x}, \mathbf{r})d\mathbf{x} \end{aligned} \quad (13)$$

Thus, convolutional interferometry on the right of equation (13) constructs the desired, one-sided estimate of $R(\mathbf{r}, \bar{\mathbf{s}})$ in equation (11) directly, without the need for time reversal (complex conjugation).

In practice, all information in the above equations are discretized in space such that the continuous surface integral over boundary S is approximately represented by a summation over seismometers at locations $\mathbf{x}_i \in S$. Each seismometer occupies the space $\Delta\mathbf{x}_i$, which, in one dimension, is the sum of half distances to the next seismometer on either side (see Figure 3a), while in two dimensions, $\Delta\mathbf{x}_i$ represents the surface area of the portion of space closer to that seismometer than neighboring seismometers (see shaded polygons in Figure 3b). We can thus rewrite equations (12) and (13) as

$$R(\mathbf{r}, \bar{\mathbf{s}}) = \int_{\mathbf{s} \in F} T(\mathbf{s})G(\mathbf{r}, \mathbf{s})d\mathbf{s} \cong \frac{2jk}{\omega\rho} \sum_{i=1}^n R^*(\mathbf{x}_i, \bar{\mathbf{s}})G(\mathbf{x}_i, \mathbf{r})\Delta\mathbf{x}_i \quad (14)$$

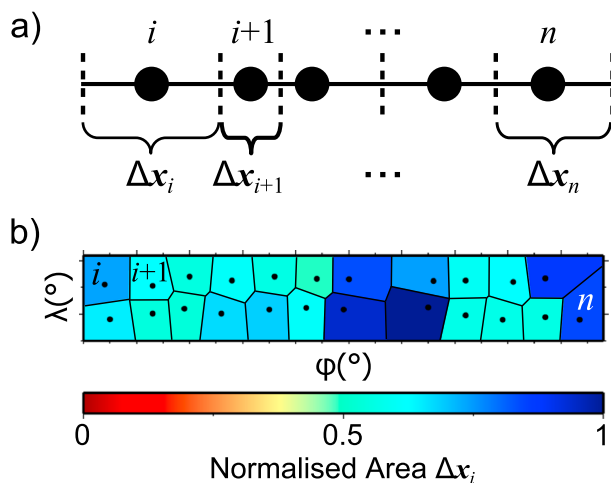


Figure 3. Illustrations of the discretization of equation (12) or equation (13) for seismometers (black circles) at positions $i \dots n$ located (a) along a 1-D line such that $\Delta \mathbf{x}_i$ is the sum of half distances to the next seismometer on either side and b) within a 2-D latitude/longitude (λ/ϕ) grid such that $\Delta \mathbf{x}_i$ is the surface area of the portion of space closer to that seismometer than neighboring seismometers. In Figure 3b the cells (polygons) have been shaded according to their size, normalized to the largest cell.

and

$$R(\mathbf{r}, \bar{\mathbf{s}}) = \int_{\mathbf{s} \in F} T(\mathbf{s}) G(\mathbf{r}, \mathbf{s}) d\mathbf{s} \quad (15)$$

$$\cong \frac{2jk}{\omega \rho} \sum_{i=1}^n R(\mathbf{x}_i, \bar{\mathbf{s}}) G(\mathbf{x}_i, \mathbf{r}) \Delta \mathbf{x}_i$$

where $R(\mathbf{x}_i, \bar{\mathbf{s}})$ is the earthquake recording at the seismometer at location \mathbf{x}_i , and the same discretization (summation notation $\sum_{i=1}^n \dots \Delta \mathbf{x}_i$) can be applied to all other continuous integrals over boundary S described above. Thus, we evaluate all integrals using a summation over available receivers, but when we discuss the theory above in the text, we continue to refer to integration as this is the underlying correct operation.

The extent to which this discretization affects the final SRI seismograms is dependent on the frequency content of the data and the spatial sampling of seismometers on the receiver boundary

S . Despite all of these assumptions (i.e., restricted boundaries, stationary-phase approximations, and discretization of the integrals), *Curtis et al.* [2012] have shown that the SRI method is able to reconstruct reasonably accurate earthquake seismograms retrospectively. Herein we test this method further by performing SRI over three different length scales and include both active source and earthquake seismology examples.

3. Application at Engineering Seismology Scale

We applied correlation-correlation SRI to construct the seismogram between an active source and a number of receivers in a small exploration or engineering scale seismic experiment performed in the field beside Schlumberger Gould Research in 2010 [*Duguid et al.*, 2011]. The acquisition geometry is shown in Figure 4: active seismic sources consisting of an accelerated weight drop were placed at intervals of 4 m along the running-track-shaped boundary S' . This boundary encloses a grid of receivers at locations \mathbf{r}_i , some of which we use as target sensors, and a receiver line S which acted as the backbone array in this case. Active shots were also recorded at all receiver positions from a source at location \mathbf{s} . Our goal is to construct seismograms from source \mathbf{s} on target receivers \mathbf{r}_i using SRI and compare the results to the real recordings.

We constructed the seismograms between source \mathbf{s} and receivers \mathbf{r}_i by applying SRI using equations (6) and (7) and without using the direct recordings of the source on \mathbf{r}_i . Thus, we simulate the case where the source at \mathbf{s} was fired before or after the period during which the receivers at \mathbf{r}_i were installed and activated, and hence where the source was only recorded on the backbone receiver boundary S . This was achieved by first using seismic energy propagating from sources on boundary S' to estimate the Green's function propagators between \mathbf{r}_i and each \mathbf{x} on S using inter-receiver interferometry in equation (6), thus turning receivers \mathbf{r}_i into virtual sources recorded by receivers at \mathbf{x} on S . We then redatum the signals from the backbone array S to the target sensors \mathbf{r}_i using inter-source interferometry in equation (7), turning the virtual sources at \mathbf{r}_i into virtual receivers.

The active-source data were recorded at 250 Hz over a time period of 4 s. As different types of geophones were deployed during acquisition (with responses centered at 4.5 Hz, 10 Hz, and 14 Hz in the target sensors, and at only 4.5 Hz at receiver line S), transfer functions from 4.5 Hz to 10 Hz, and from 14 Hz to 10 Hz were estimated from the recorded data and applied to the 4.5 Hz and 14 Hz data before any subsequent processing [*Duguid et al.*, 2011]. In order to ensure coherency in the frequency content across all receivers,

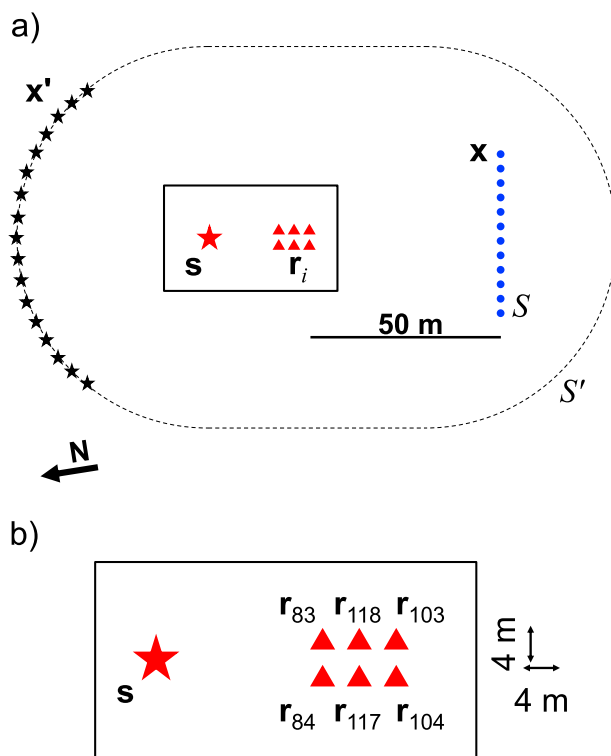


Figure 4. Geometry for the small-scale seismic experiment. (a) Active sources are located along the dashed boundary S' (small/black stars) and at position s (large/red star). Receivers are located along line S (circles: every second receiver is shown here for clarity) and at points r_i (triangles) close to the source at s . Only those boundary sources located approximately around the stationary-phase region of S' are used (small/black stars). (b) Magnified view of the active source and the target receivers marked by triangles with receiver numbers shown in the numbering scheme of *Duguid et al.* [2011]: results for these receivers are shown in Figure 5.

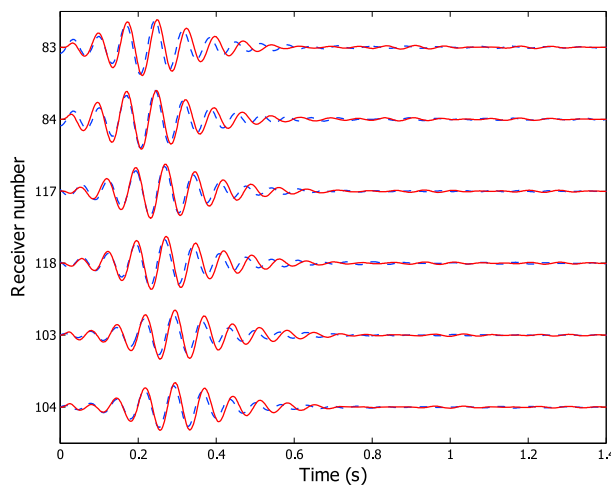


Figure 5. Comparison of surface wave (ground roll) seismograms constructed using SRI (solid/red traces) with the real recordings (dashed/blue traces) at the target sensors r_i shown in Figure 4b. All seismograms are band passed in the frequency range 8 Hz – 15.5 Hz, chosen because that range contained all dominant amplitudes that were common to all recordings at x and r_i in Figure 4.

the data from boundary S' was filtered between 8 Hz and 22 Hz before the inter-receiver step. In accordance with the stationary-phase principles of *Sniieder* [2004], only a subset of boundary sources that were assumed to provide a constructive contribution to the integrand in equation (7) were used to construct the inter-receiver Green's functions (see the small/black stars in Figure 4a). Before the inter-source step, a second filter (8 Hz – 15.5 Hz) was applied to the signals recorded by the backbone array and to those recorded from the active source s at the receivers r_i . This was the only frequency band with significant energy that overlapped between all recorded signals, which thus limits the results to a narrow frequency band.

The results of SRI for the six receivers r_i are shown in Figure 5: all seismograms are cut to 1.4 s in length and are normalized to their absolute maximum amplitude. The dominant arrival is the emerging surface wave (ground roll) which can be seen to move out from the source for increasingly distant receivers. The match is not perfect, and this is likely partly because the equations derived herein for correlational interferometry assume a non-attenuating medium which is an approximation, and that boundaries S' of sources and S of receivers extend downwards into the subsurface. Also, similar weight drop sources were used at locations x' and s : thus, in the first step of interferometry both Green's functions on the right of equation (6) are in fact convolved with the source time function, and the result on the left will therefore be multiplied by the source power spectrum. This extra factor is then multiplied into the SRI result in equation (7) but will not be present in the real recording. Of course, since we have both the real recordings and the SRI seismograms at receivers r_i in this case, in principle we could divide one by the other to obtain the source power spectrum [*Behura and Sniieder, 2013*]. We do not implement this here as first it assumes a non-attenuative medium, and second we focus on testing

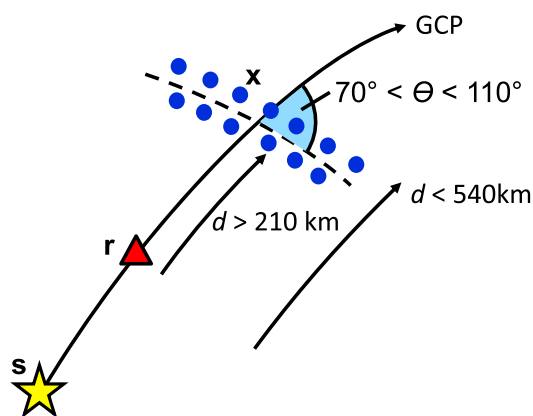


Figure 6. Schematic diagram illustrating the spatial criteria specified in section 4.1 for a source *s* (star), target sensor *r* (triangle), band of backbone seismometers *x* (circles), and great circle path (GCP) passing between *s* and *r*. The criterion used in section 4.3 that the backbone seismometers should lie between a distance of 210 km and 540 km from the target sensor is also indicated, as is the intention that the intersection angle Θ should be between 70° and 110° .

the case where we do not have any direct recordings at *r*. Finally, in this controlled small-scale example the SRI reconstructions are narrow band signals with a low-frequency content compared to other industrial surveys (8 Hz–15.5 Hz). This has implications for the use of such SRI seismograms for subsurface imaging as spatial resolution will be low.

Nevertheless, in all cases the match between the real and SRI traces is reasonably good, showing the reliability of the method in a controlled experiment and when an ideal geometry of sources and receivers is available. In the next sections, we apply the principles of SRI and retrospective seismology to less controlled scenarios in earthquake seismology, showing the potential of this method when the distribution of sources and receivers is far from perfect.

4. Applications at Earthquake Seismology Scale

We now apply correlation-correlation SRI and correlation-convolution SRI in two earthquake seismology settings using ambient wavefield fluctuations recorded on a backbone array of seismometers *x* and on target sensors *r*, as described by equations (9), (12), and (13). We reconstruct the seismograms from two earthquakes retrospectively, on two target sensors (seismometers) that were deployed, and then removed before the earthquakes occurred, and thus which did not record the events. To test the robustness of the method, we also reconstruct the event seismograms on up to seven other target sensors that were operational at the time that the earthquakes occurred and compare the reconstructed seismograms with those actually recorded. The quality of the match between the real and SRI seismograms constructed at any one target sensor is quantified by calculating the correlation coefficient over the lengths of the traces displayed in Figures 8a, 10, 12, and 14.

4.1. Spatial Sampling and Station Recording Criteria

A search of the dates of installation of all USArray stations was carried out to determine the number of seismometers deployed at the time of a catalogue of earthquakes. Of these seismometers, those that satisfy the following spatial criteria were selected for the backbone seismometer array (see Figure 6 for a schematic illustration of these criteria):

1. The backbone seismometer array consists of at least two parallel lines of approximately regularly spaced seismometers (using a laterally extended band of seismometers rather than a single line compensates to some extent for the lack of seismometers at depth, which otherwise may lead to spurious arrivals due to inter-mode surface wave correlations [Halliday and Curtis, 2008]).
2. A great circle path (GCP) from the earthquake epicenter intersects the seismometer array approximately perpendicularly—at a local intersection angle of between 70° and 110° .
3. The same GCP intersects at least one target seismometer *r* that did not record the event.
4. Seismometers in the backbone array are operational at the time the event occurred, and all seismometers have at least 6 months in common of ambient seismic noise recordings.

For backbone and target seismometers that satisfy the above criteria, instrument response files and up to 2 years of vertical component, daily ambient noise records sampled at four samples per second were downloaded from the Incorporated Research Institutions for Seismology (IRIS) database. Ambient noise was downloaded from January 2009 to December 2010 depending on the deployment history of the seismometers selected. Both summer and winter noise data were thus downloaded, reducing the bias in ambient wavefield directivity from temporal (seasonal) dependencies. In the figures herein we schematically represent the noise sources by small black stars in the nearby oceans for simplicity, but note that their actual

origin can be far further afield [Shapiro *et al.*, 2006; Yang and Ritzwoller, 2008; Kedar, 2011; Zeng and Ni, 2014]. Earthquake recordings made at the selected backbone seismometers were also downloaded. Each earthquake trace began at the origin time of the event and was 8000 s in length.

4.2. Data Processing and Methodology

Processing of the ambient seismic noise data and earthquake recordings is carried out following the methods of Bensen *et al.* [2007]. For each daily noise record and each earthquake recording made on the backbone seismometer array, the instrument response, mean and trend are removed and bandpass filters with corner frequencies at 0.01 Hz and 1 Hz are applied. This frequency range is kept as broad as possible at this stage to ensure that no important frequencies are lost early on in the noise processing sequence.

4.2.1. Inter-Receiver Interferometry Step

Temporal normalization is applied to each daily noise record to reduce the effects of large amplitude signals on the cross correlations. Such signals are caused by earthquakes, nonstationary noise sources near to the station, and instrumental irregularities [Bensen *et al.*, 2007]. We use the 1 bit normalization method which replaces all positive amplitudes with +1 and all negative amplitudes with -1. This is the most aggressive temporal normalization method described by Bensen *et al.* [2007] as it removes all amplitude information by keeping only the sign of the raw signal. It has been shown to improve the signal-to-noise ratio (SNR) of ambient noise Green's function estimations [Derode *et al.*, 2003b] and has been used in a number of ambient seismic noise studies [e.g., Shapiro and Campillo 2004; Shapiro *et al.*, 2005; Stehly *et al.*, 2007; Nicolson *et al.*, 2012, 2014].

Finally, spectral normalization (whitening) is applied to the filtered, 1 bit normalized noise records. This targets the spectrally biased nature of ambient seismic noise and reduces the effects of persistent monochromatic noise sources, such as the 26 s peak associated with a narrowband noise source in the Gulf of Guinea [Shapiro *et al.*, 2006; Bensen *et al.*, 2007].

For each station pair between a backbone array seismometer and a target sensor, the daily ambient noise recorded on the array seismometer \mathbf{x} is cross correlated with the ambient noise recorded on the target sensor \mathbf{r} to produce a noise correlation function. All daily correlation functions computed between each station pair are stacked to construct a single estimate of the Green's function, $G_H(\mathbf{x}, \mathbf{r})$. At positive times we obtain an approximation to $G(\mathbf{x}, \mathbf{r})$, the response that would have been recorded at the backbone array seismometer \mathbf{x} if an impulsive source had been fired at the location of the target sensor \mathbf{r} (as in equation (9)). The target sensor \mathbf{r} is thus turned into a virtual source. To obtain the one-sided Green's function, the acausal part of each stacked correlation function is time reversed and added to the causal part to create our final approximation to $G(\mathbf{x}, \mathbf{r})$. Each estimated Green's function is cut to 8000 s. A second band-pass filter with corner frequencies at 0.02 Hz and 0.1 Hz is then applied to both the estimated Green's functions and the earthquake recordings. This restricts all data to the same length (in time) and to the same frequency band, within which we expect a significant overlap in energy between all signals.

4.2.2. Inter-Source Interferometry Step

The earthquake signal recorded at an array seismometer $R(\mathbf{x}, \mathbf{s})$ is cross correlated with the estimate of $G(\mathbf{x}, \mathbf{r})$. According to Curtis *et al.* [2012] and equation (12), if we integrate the results over the backbone receiver array for varying \mathbf{x} on S , the acausal part of the constructed seismogram approximates the earthquake response that would have been recorded at the target sensor \mathbf{r} if the sensor had been deployed at the time of the event. When using correlation-convolution SRI, the earthquake signals recorded at \mathbf{x} are convolved with the estimate of $G(\mathbf{x}, \mathbf{r})$ as in equation (13). Integration over all backbone array seismometers constructs our estimate of the true response at \mathbf{r} from the earthquake source at \mathbf{s} .

The integrand of equation (12) (or equation (13)) constructed on seismometers located around the center of the backbone array contribute most to the final reconstructed seismogram. These seismometers lie within the stationary-phase regions of the receiver boundaries and are highlighted schematically by the thick grey lines in Figures 2a and 2b [Snieder, 2004]. Since the receiver arrays employed at these larger scales are usually irregularly spaced, we found it necessary to perform an interpolated sum over \mathbf{x} in this interferometry step. From here onward we shall thus consider the discretized forms of the inter-source interferometric equations as shown by equations (14) and (15). The interpolation should be such that it improves the approximation of this summation to the integrations in equations (12) and (13). Hence, where there is high receiver density, each receiver should individually contribute less to the integration (summation) than when the receivers are sparsely distributed.

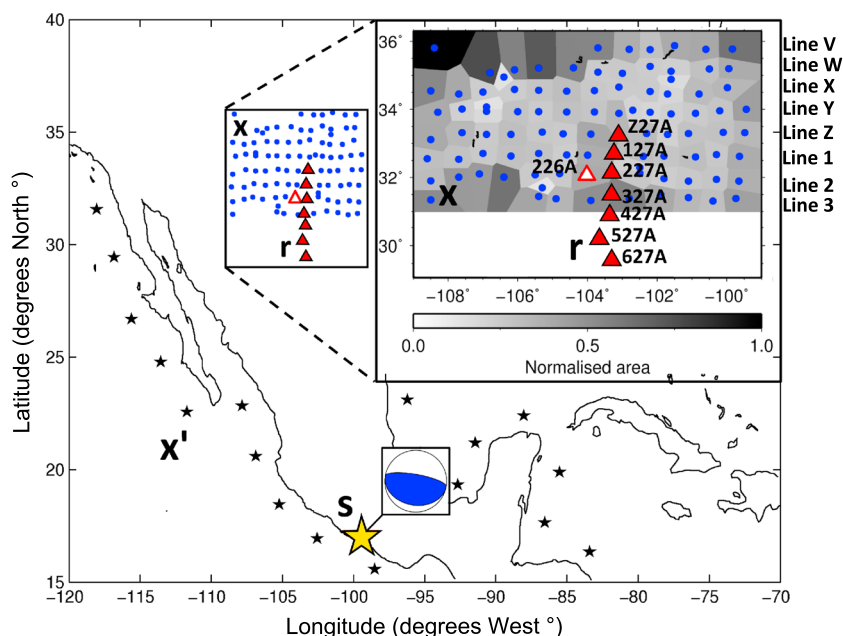


Figure 7. Source and receiver geometries used to reconstruct virtual seismograms of the 27 April 2009 M 5.8 Mexico earthquake (large star with source mechanism) using correlation-correlation SRI (Figure 2a). Ambient noise fluctuations from source locations such as x' (small stars positioned schematically in oceans) are recorded on the backbone seismometer array x (circles) and at the eight target sensors r (filled and unfilled triangles) located within New Mexico. The backbone array consists of eight approximately parallel lines of seismometers from Line V in the North of the array to Line 3 in the South (the letters derive from station notation employed in naming the USArray Transportable Array). Two-line combinations of the backbone array seismometers are used to reconstruct virtual earthquake seismograms at each target sensor by interpolating interferometric integrands across the Voronoi cells (polygons: shaded according to their area). To reconstruct the virtual earthquake seismogram at sensor Z27A, only those seismometers along lines V and W comprise the backbone array; to reconstruct the virtual earthquake seismogram at sensor 127A, only seismometers along lines W and X comprise the backbone array; and so on, until the virtual earthquake seismogram at sensor 627A is reconstructed using an array comprised of seismometers from Lines 2 and 3 only.

To invoke the summations in equations (14) and (15) more precisely, we embed each backbone seismometer array within a rectangular patch of 2-D spatial Voronoi cells, such that seismometer coordinates become Voronoi cell centers (for example, see inset in Figure 7). The spatial area of each Voronoi cell is used as the discretization factor Δx_i in the summands of equations (14) and (15) for seismometer x_i at that cell's center. In addition, the summands are multiplied by a tapered cosine weighting function to remove effects due to the finite boundary length available (see below). Original and adapted codes by *Sambridge et al.* [1995] and *Sambridge* [1999a, 1999b] are used to calculate Voronoi cell areas in these computations.

Each rectangular patch (like that in the inset in Figure 7) is divided into a regular grid of square cells of side length approximately 100 km. Each such cell is assigned the value of the summand of equation (14) or equation (15) from the seismometer x_i at its Voronoi cell's center. Instead of summing over seismometers in the backbone array to approximate the summations in equations (14) and (15), we sum over this regularly spaced grid of "interpolated" seismometers. First though, a cosine-tapered window is applied to the rectangular grid in the x and y directions, such that the first and last 25% of the points in each direction are weighted by half cosines normalized to lie in the interval $[0, 1]$, and the middle 50% of points are left unchanged. This acts to reduce the edge effects (an effect that would otherwise be imposed by our own rectangular boundary selection) and ensures that contributions from seismometers toward the center of the array (i.e., within the approximate stationary-phase region) provide a stronger contribution to the final summation than seismometers toward the edges. Finally, we sum the taper-weighted values of the summands over all cells within the 2-D rectangular patch to construct the final estimate of the recording of event s at sensor r . This entire two-step process approximates the application of SRI to the recorded data. Note that this interpolation method uses zeroth-order (constant) Voronoi cell interpolation [*Sambridge*, 1999a] as represented by the summations in equation (14) or equation (15). A more accurate method of

interpolation could be obtained by expanding the interpolation within each Voronoi cell to higher orders (e.g., using bilinear interpolation between each cell and neighboring cells).

Finally, to compare the real and virtual seismograms directly we apply a band-pass filter within the frequency band where both the earthquake and noise spectra overlap with significant energy. Here we present the data within the band 0.04 Hz to 0.06 Hz as these intermediate frequencies performed better on average than higher (0.08 Hz to 0.1 Hz) or lower (0.02 Hz to 0.04 Hz) frequencies when the spatial sampling of the backbone array, and thus, the discretization in equation (14) or equation (15) varied. Unfortunately in this study, the recovered frequency content of the SRI seismograms is very low which currently prevents the virtual seismograms from being used for high-resolution imaging.

Within the 0.04 Hz to 0.06 Hz frequency band, there was only a marginal improvement in results from using two lines of seismometers within the backbone array compared to a single line of seismometers. However, if only a single line of seismometers is available and spatial sampling along that line is sparse, higher frequencies (0.08 Hz to 0.1 Hz) were found to perform marginally better than intermediate values. This is surprising as the Nyquist sampling criterion along the boundary would suggest that a denser backbone array is required to capture the characteristics of a higher-frequency wavefield. This effect may therefore merit further study. Herein we have consistently used two lines of backbone seismometers as there is little variation in the spatial sampling of the arrays chosen for each individual SRI reconstruction in most of our examples. However, when seismometers *are* missing we observe that Voronoi interpolations help to account for this irregularity by spatially averaging the existing data.

4.2.3. Quality Control

Two quality control checks are carried out following the cross correlation of ambient noise in the inter-receiver step above, based on the signal-to-noise ratio (SNR) of each result. We define the SNR as the ratio of the absolute maximum amplitude within a signal window to the root-mean-square (RMS) value of a noise window. The signal window spans a time period within which we expect a surface wave arrival, and the noise window is defined such that it is temporally later than this signal window.

After the daily noise correlation functions have been produced for each \mathbf{x} in equation (9), an approximate surface wave arrival time τ is calculated for each station pair using the interstation distance and a mean group velocity of 3.25 km/s. This group velocity was chosen using the group velocity curves provided by *Bensen et al.* [2008], in which the authors studied similar interstation USArray paths. The signal window is chosen to span the range $(\tau - 250 \text{ s})$ to $(\tau + 250 \text{ s})$, and a 500 s noise window is defined to follow this signal window. The SNR of each daily correlation function is then calculated. Those with a SNR value ≥ 4.8 are normalized (divided) by the RMS value of their signal window, while those with a SNR value between 2 and 4.8 are normalized by their absolute maximum amplitude as we found this better removed any spurious peaks of energy in lower SNR signals. Any daily correlation functions with SNR values ≤ 2 are removed from the study altogether.

A second SNR check is carried out after the daily correlation functions have been stacked and the inter-receiver Green's functions have been estimated in equation (9). Those with a SNR value ≥ 15 are normalized by the RMS value of their signal window, whilst those with a SNR value between 3 and 15 are normalized by their absolute maximum amplitude. If any have a SNR value ≤ 3 at this stage, they are removed.

The above set of SNR thresholds were defined following a series of trial and error tests on many data. For example, trial and error tests on the daily correlation functions identified a possible top SNR limit of between 4.5 and 5, with the majority of "good" signals having a SNR value greater than 5. However, to encompass those correlation functions whose signals were still strong in comparison to the background noise level (SNR values between 4.5 and 5), an intermediate value of 4.8 was chosen. For the majority of daily files with SNR values less than 4.8, the signal was not necessarily clearly discernible from the noise by eye.

4.3. Example 2 at an Intermediate Scale

We first reconstructed the seismograms from a magnitude 5.8 earthquake on eight target sensors using a backbone array comprising 93 seismometers that satisfied the spatial sampling criteria outlined above, and correlation-correlation SRI (equations (9) and (14) and Figure 2a). The backbone array and the eight target sensors at which seismograms were reconstructed are shown in Figure 7. Earthquake signals were reconstructed at each of the eight sensors using combinations of seismometers on two lines located on average between approximately 210 km and 540 km from the sensors: the caption in Figure 7 states which lines

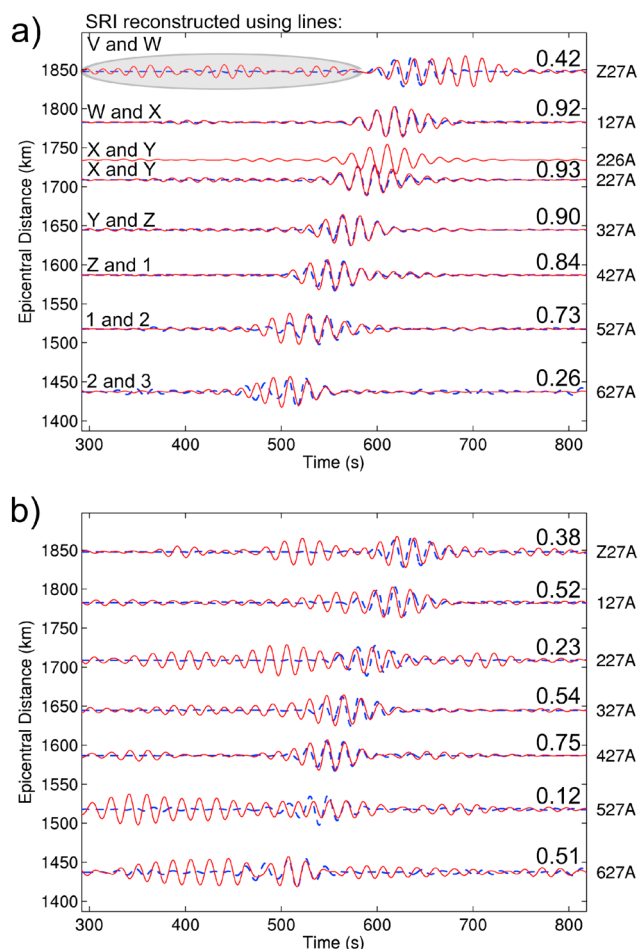


Figure 8. Comparison of seismograms for the *M* 5.8 Mexico earthquake constructed using correlation-correlation SRI (solid/red traces) with the real recordings (dashed/blue traces) at target sensors Z27A to 627A and at 226A in Figure 8a. At 226A there is no real recording of the event. The quality of the match between the real and SRI seismograms is quantified by the correlation coefficient, stated on the right above each trace. (a) SRI seismograms are constructed by integrating over two-line combinations of seismometers within the Voronoi cells shown in Figure 7 as described in the caption to that figure and stated here on the left above each trace. (b) The SRI integral in equation (12) is approximated by performing a direct summation over all backbone seismometer locations rather than as an interpolated sum over Voronoi cells. The grey-shaded ellipse in Figure 8a highlights the spurious, nonphysical arrivals that occur prior to the main surface wave arrivals constructed at target sensor Z27A for comparison with Figure 10.

correlation coefficients reach values up to 0.93. Sensor 226A (unfilled triangle in Figure 7), was active prior to the earthquake but was removed from its site before the earthquake occurred. The reconstruction at 226A is thus a new virtual seismogram constructed at a seismometer location selected retrospectively. This also demonstrates that even after sensors have been removed, virtual seismograms can be obtained at their previous locations provided that the backbone array remains intact and the properties of the medium have not changed significantly in the elapsed time between the deployment of the seismometers and the occurrence of the event [Curtis *et al.*, 2012].

Figure 8b shows the results if the integrand in equation (12) is approximated by a simple summation of the integrands calculated at each station \mathbf{x}_i on S , that is if the Voronoi cell area $\Delta \mathbf{x}_i$ in equation (14) is omitted. The quality of seismogram reconstructions deteriorates significantly, as discussed further below.

were used for which target sensor. On average 22 backbone array seismometers were used for each reconstruction. Figure 7 (inset) shows the locations of the array seismometers within their 2-D spatial Voronoi cells. The number of seismometers available for each reconstruction varies depending on the deployment history of the seismometers, and the outcome of the quality control checks described above. Each remaining backbone seismometer became a Voronoi cell center, and two-line combinations of Voronoi cells were used to interpolate across grids of square cells, the grid having dimensions between 1.5° and 1.8° in latitude and 7.7° and 9.9° in longitude. We assume that the backbone array seismometers chosen include the stationary-phase points of the receiver boundary S .

The final SRI seismograms were then compared with the real recordings of the event that existed on seven of the target sensors. SRI reconstructions and real earthquake recordings at all target sensors are plotted within the frequency band 0.04 Hz to 0.06 Hz as a function of epicentral distance in Figure 8a. All seismograms are normalized to their absolute maximum amplitude and the quality of the match between the real and SRI seismograms in the windows shown is quantified by the correlation coefficient as stated on the right of the figure, above each trace. The moveout of the main surface wave arrival with distance is clearly visible. Also, the phase of the main arrivals estimated using SRI are in good agreement with the actual recorded seismograms at the same sensor (where the latter exists) and

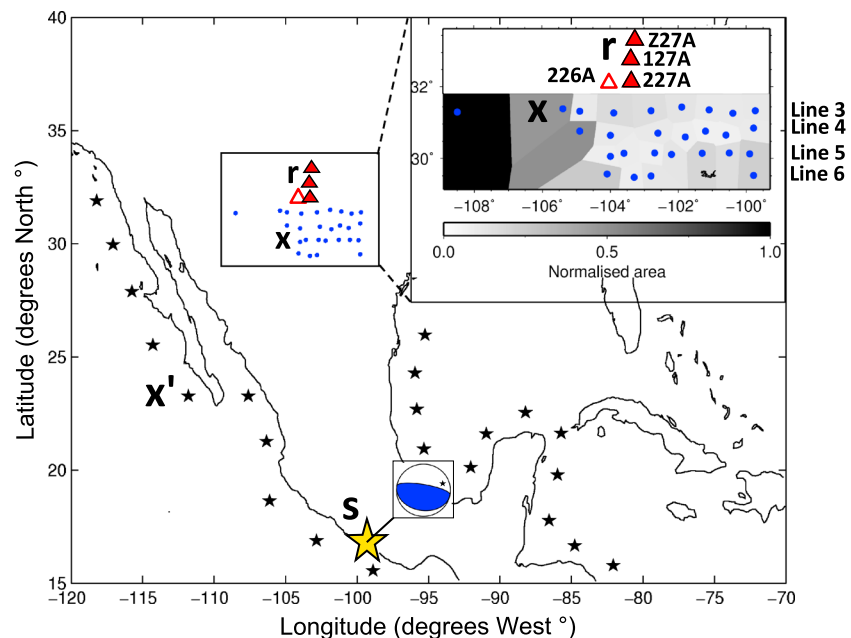


Figure 9. Source and receiver geometries used to reconstruct virtual seismograms of the 27 April 2009 *M* 5.8 earthquake in Mexico using correlation-convolution SRI (Figure 2b). Key as in Figure 7. Two-line combinations of backbone array seismometers are used to reconstruct virtual earthquake seismograms of the earthquake at sensors Z27A, 127A, 227A, and 226A by interpolating the interferometric integrands in equations in the text over the Voronoi cells shown in the inset (shaded polygons). To reconstruct the virtual earthquake seismogram at sensor Z27A, only those seismometers along Lines 3 and 4 comprise the backbone array; to reconstruct the virtual earthquake seismogram at sensor 127A, only seismometers along Lines 4 and 5 comprise the backbone array, and finally, the virtual earthquake seismograms at sensors 226A and 227A are constructed using an array comprised of seismometers along Lines 5 and 6 only.

Next we used correlation-convolution SRI (equations (9) and (15) and Figure 2b) to reconstruct earthquake seismograms at target sensors Z27A, 127A, 227A, and 226A using the backbone array shown in Figure 9 and two-line combinations of the Voronoi cells shown in the inset to Figure 9 and described in the caption to that figure. The SRI seismograms are compared with the real recordings of the earthquake at the target

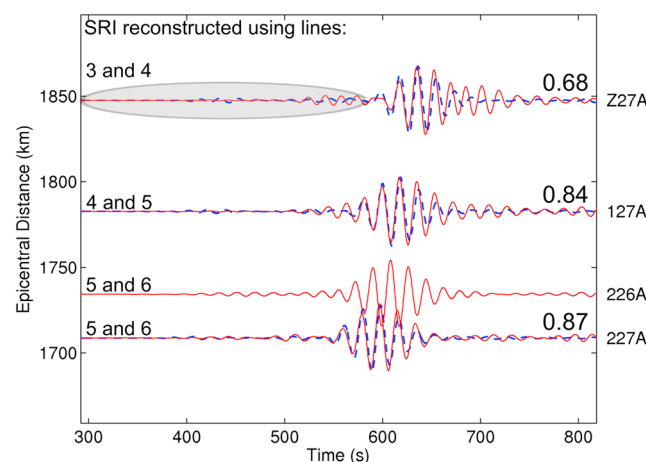


Figure 10. Comparison of seismograms for the *M* 5.8 Mexico earthquake constructed using correlation-convolution SRI (solid/red traces) with the real recordings (dashed/blue traces) at target sensors Z27A, 127A, 227A, and 226A. Key as in Figure 8. The geometry for this correlation-convolution approach to SRI is shown in Figure 9. The grey-shaded ellipse highlights the region in which higher-amplitude spurious, nonphysical arrivals were reconstructed when using correlation-correlation SRI (see Figure 8, top trace).

sensors in Figure 10. We again observe clear surface wave arrivals in the SRI seismograms that are in phase with the real recordings at the target sensors (where the latter exists) and which agree well with the top four traces in Figure 8a which are constructed at the same target sensors using correlation-correlation SRI. Thus, we verify that both correlation-correlation and correlation-convolution SRI can be used for this form of retrospective seismology, and the method used depends on the backbone array geometry available. Furthermore, the spurious events in the correlation-correlation SRI seismograms that occur prior to the main surface wave arrivals disappear when one uses the correlation-convolution approach. For example, compare the SRI reconstructions at target sensor Z27A in Figure 8a to the same sensor

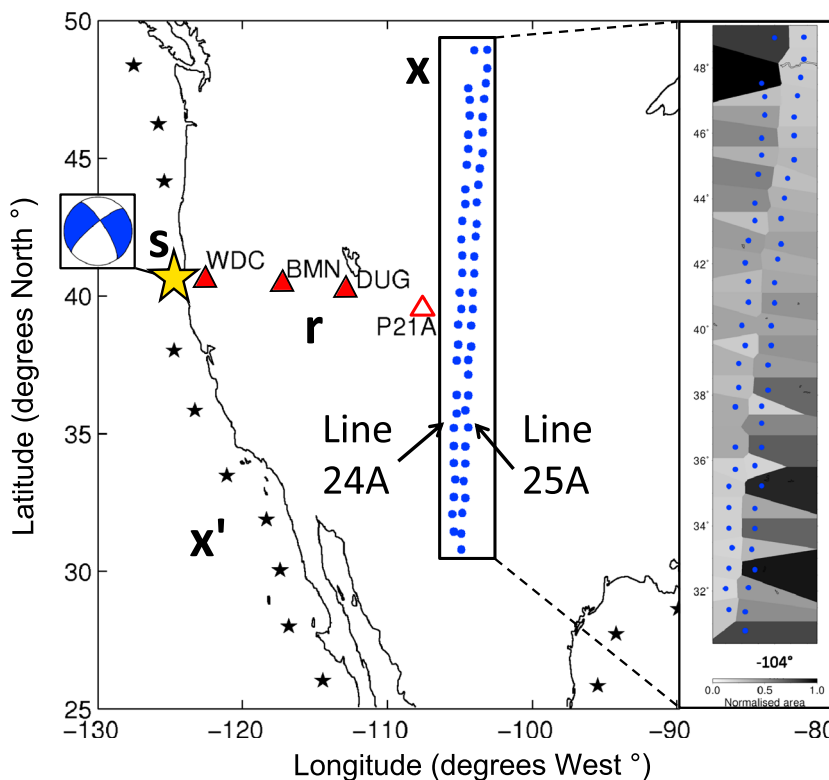


Figure 11. Source and receiver geometries used to reconstruct the virtual seismograms of the 10 January 2010 M 6.5 earthquake that occurred off the coast of California using correlation-correlation SRI (Figure 2a). Key as in Figure 7. The backbone array consists of two adjacent lines of seismometers with Line 24A on the left and Line 25A on the right. Combinations of the 57 seismometers within the array are used to reconstruct virtual earthquake seismograms at target sensors WDC, BMN, DUG, and P21A by interpolating interferometric integrands across the Voronoi cells shown in the inset (shaded polygons).

in Figure 10 (top trace). When using correlation-correlation SRI, artifacts are introduced between approximately 300 s and 550 s (see grey ellipse in Figure 8a) and this lowers the correlation coefficient of the SRI seismogram (a value of 0.42 is obtained). These nonphysical arrivals are not constructed when using the correlation-convolution approach (see grey ellipse in Figure 10), and the correlation coefficient subsequently increases to a value of 0.68.

4.4. Example 3 at the Largest Scale

Finally, we created a large-scale example designed to challenge the method. Correlational interferometry as described herein contains an underlying assumption of zero attenuation, and as propagation distance increases, this assumption becomes increasingly questionable. We also wanted to test the method when using target sensors that lie relatively close to the earthquake source compared to the locations of the backbone array seismometers. We first reconstructed earthquake seismograms at target sensors WDC, BMN, DUG, and P21A using correlation-correlation SRI (equations (9) and (14) and Figure 2a) and large arrays of backbone seismometers that spanned almost 20° in latitude (see Figure 11 and the inset to that figure for the locations of the seismometers within 2-D spatial Voronoi cells). The seismometers were located along Lines 24A and 25A of the USArray Transportable Array network and a total of 54, 55, 56, and 51 array seismometers were used as the backbone seismometers to reconstruct the earthquake seismograms at target sensors WDC, BMN, DUG, and P21A, respectively.

These virtual seismograms are shown in Figure 12a. SRI results are plotted against epicentral distance and overlain by the real earthquake recordings at these locations (where the latter exists). As for the previous example, a band-pass filter with corner frequencies at 0.04 Hz and 0.06 Hz has been applied to both the SRI reconstructions and the real recordings and all seismograms have been normalized to their absolute maximum amplitude. The main surface wave arrivals are reconstructed by SRI, but there are differences in the phase of these virtual arrivals compared to the recorded data. Artifacts are present both before and after

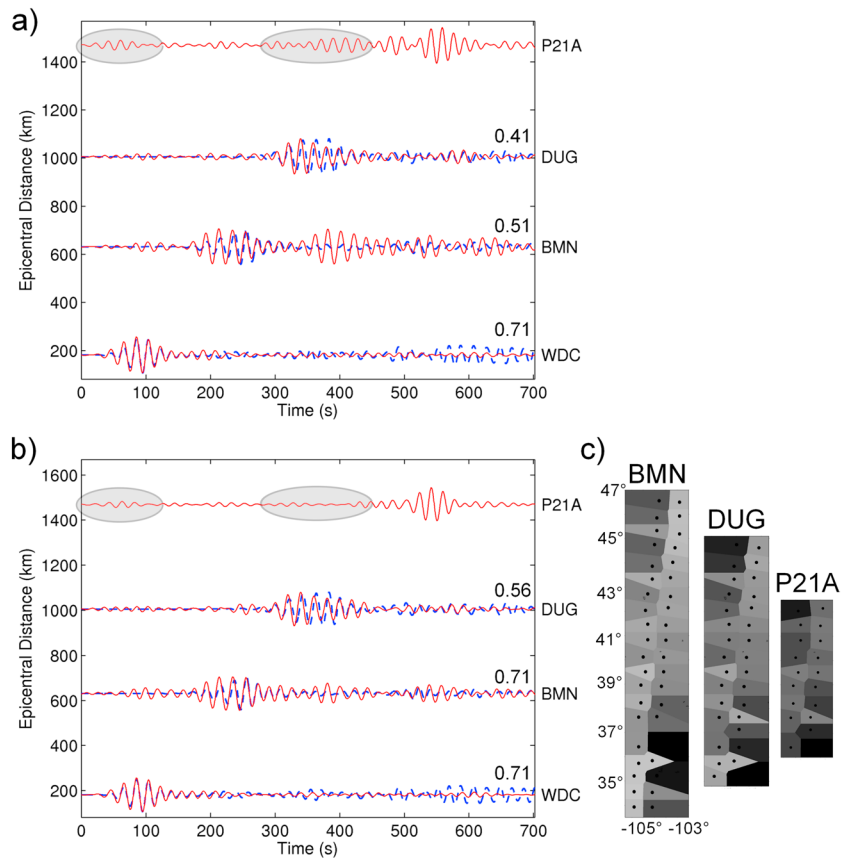


Figure 12. (a) Comparison of seismograms for the M 6.5 earthquake that occurred off the coast of California constructed using correlation-correlation SRI (solid/red traces) with the real recordings (dashed/blue traces) at target sensors WDC, BMN, DUG, and P21A. At P21A there is no real recording of the event. Key as in Figure 8. Virtual earthquake seismograms are constructed using the full backbone receiver array shown in Figure 11. (b) As in Figure 12a but virtual earthquake seismograms at BMN, DUG, and P21A are constructed using spatially restricted backbone arrays consisting of seismometers whose locations are expected to better approximate the stationary-phase points of the receiver boundary S for the target sensor at r in equation (12); (c) these restricted arrays within 2-D spatial Voronoi cells are shown. The Voronoi cells are shaded according to their area as in Figure 7.

the main surface wave arrivals at sensors BMN and DUG, but we note that the best reconstruction is at target sensor WDC, which is located over 1900 km from the backbone array and within 200 km of the earthquake epicenter. The quality of the match between the real and SRI seismograms is quantified by the correlation coefficient, and we observe a maximum value of 0.71 for the reconstruction at WDC.

Target sensor P21A (unfilled triangle in Figure 11) was previously active but was removed from its site before the earthquake occurred. This seismogram is thus constructed at a truly retrospective location—a location chosen from previous seismometer locations after the event occurred. The result is shown at the top of Figure 12a and constitutes a new virtual seismogram for that receiver, from an earthquake that occurred after the receiver had been removed. The main surface wave appears to be constructed but large-amplitude nonphysical arrivals are also constructed at earlier travel times (see grey ellipses), indicating that this reconstruction is unreliable.

We propose that the largely inaccurate SRI reconstructions at target sensors BMN, DUG, and P21A are a consequence of incorrectly approximating the stationary-phase region of the receiver boundary S , i.e., fewer backbone seismometers are required on S when the backbone seismometer-target sensor distance is short [Snieder *et al.*, 2006b]. Thus, we perform correlation-correlation SRI using spatially restricted backbone arrays that consist of only those seismometers whose locations approximate the stationary-phase points of the receiver boundary S in equation (12). The arrays used are shown in Figure 12c, embedded within Voronoi cells and are used to reconstruct the SRI seismograms at target sensors BMN, DUG, and P21A as shown in Figure 12b. All backbone seismometers as shown in Figure 11 are used to construct the SRI seismogram at

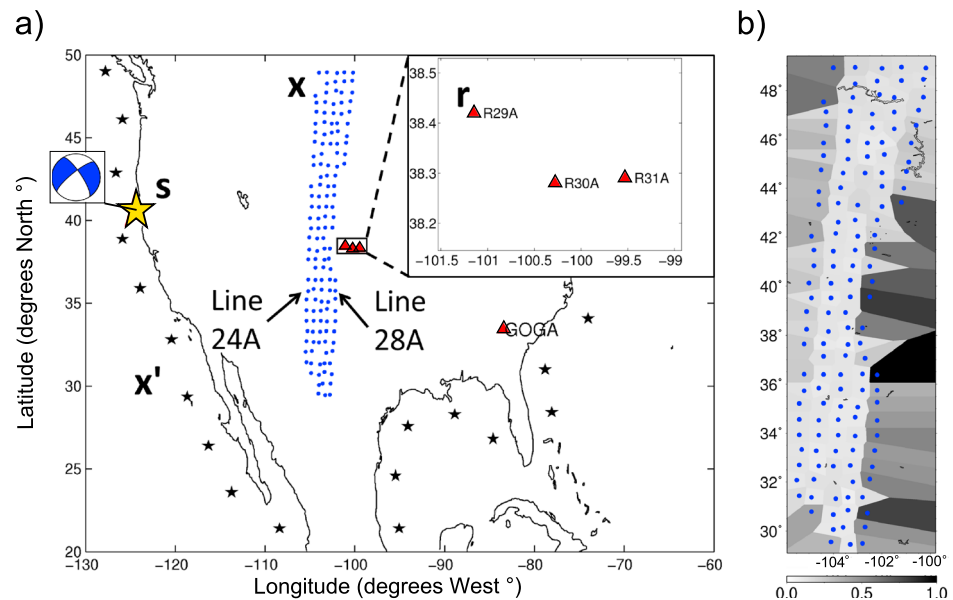


Figure 13. Source and receiver geometries used to reconstruct virtual seismograms of the 10 January 2010 M 6.5 earthquake that occurred off the coast of California using correlation-convolution SRI (Figure 2b). Key as in Figure 7. The backbone array consists of five adjacent lines of seismometers from Line 24A on the left of the array, to Line 28A on the right of the array. Two-line combinations of the backbone array seismometers are used to reconstruct virtual earthquake seismograms at target sensors R29A, R30A, R31A, and GOGA by interpolating interferometric integrands over the corresponding 2-D Voronoi cells. (b) The Voronoi cells within which the array seismometers are embedded.

target sensor WDC. Note that the SRI reconstruction at P21A requires the fewest backbone seismometers. This is a consequence of the close proximity of target sensor P21A to the backbone array in Figure 11 and thus a narrower stationary-phase region around the receiver boundary S . We observe a significant improvement in the results of correlation-correlation SRI when using the shorter backbone seismometer arrays that more accurately approximate the stationary-phase regions of S for each target sensor at \mathbf{r} in equation (12). For example, compare the SRI seismograms constructed at target sensor BMN in Figures 12a and 12b. When using all 54 seismometers in (a) the match between the real and SRI seismograms is poor as the correlation coefficient is just 0.51. This correlation coefficient increases to 0.71 in (b) when using the restricted array of only 40 seismometers to construct the SRI seismogram. Similarly, the amplitudes of the nonphysical arrivals constructed between ~ 300 s and 450 s in the SRI seismogram at target sensor P21A in (a) (grey ellipses) are significantly reduced when using the shorter array. We found that to construct the SRI seismogram at a given target sensor, only those backbone array seismometers located at distances within ~ 250 km of the shortest backbone seismometer-to-target sensor distance should be used.

Next we used correlation-convolution SRI (equations (9) and (15) and Figure 2b) to reconstruct earthquake seismograms at four additional target sensors (sensors R29A, R30A, R31A, and GOGA). Again, we begin by using large backbone arrays (as shown in Figure 13) to construct the SRI seismograms. We extend the source-receiver geometry to target sensor GOGA located up to 2420 km from the backbone seismometer array and over 3700 km from the earthquake epicenter. Note that since processes of convolution do not involve time reversal (complex conjugation), convolutional interferometry does not have an implicit assumption of zero attenuation [Halliday and Curtis, 2009]. In this example, however, noise-based correlational interferometry in equation (9) is still used to construct the SRI propagators $G(\mathbf{x}, \mathbf{r})$; hence, this correlation-convolution approach to SRI still has an implicit assumption of zero attenuation, which is questionable at these propagation distances.

The SRI seismograms are plotted in Figure 14a and compared with the real recordings of the earthquake at those same sensors. Despite the assumption of lossless media made herein, the main surface wave arrivals can be traced across all target sensors, and the SRI seismograms are in reasonable agreement with the real recordings at target sensors R29A, R30A, and R31A. The quality of these matches is quantified by the

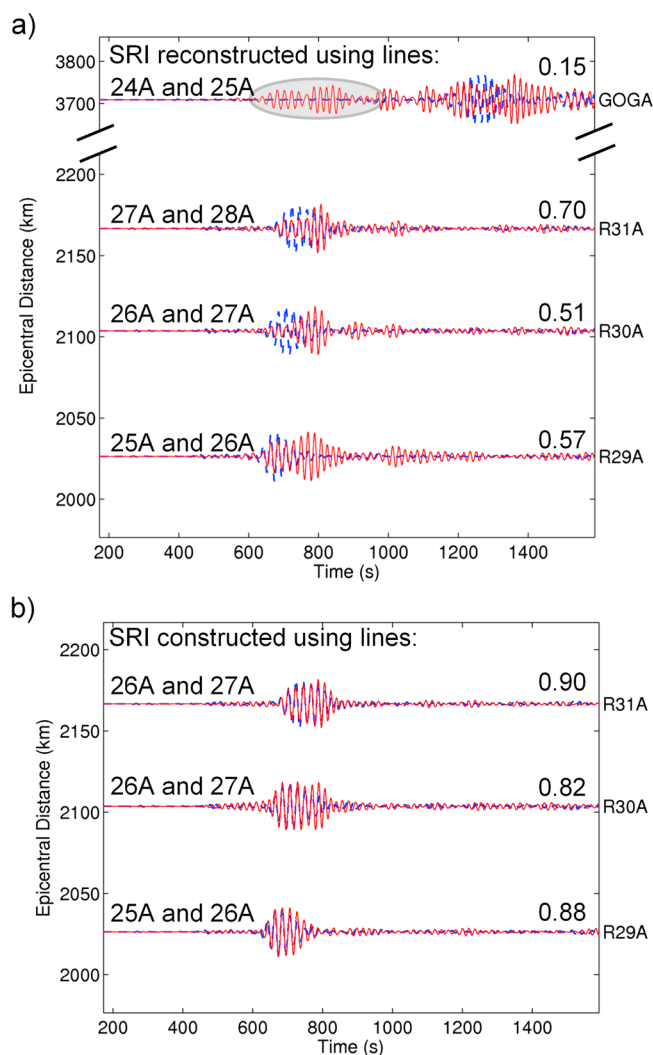


Figure 14. (a) Comparison of seismograms for the *M* 6.5 earthquake that occurred off the coast of California constructed using correlation-convolution SRI (solid/red traces) with the real recordings (dashed/blue traces) at target sensors R29A, R30A, R31A, and GOGA. Key as in Figure 8. Virtual earthquake seismograms are constructed using two-line combinations of the full backbone receiver array shown in Figure 13. (b) As in Figure 14a but for target sensors R29A, R30A, and R31A only. Virtual earthquake seismograms are constructed using restricted backbone arrays consisting of only 11 or 12 seismometers that are located along the central region of the receiver lines stated on the left above each trace and displayed in Figure 13.

was observed by further limiting the array. The main surface wave is reconstructed but is of a similar amplitude to earlier spurious arrivals at ~800 s (see grey-shaded ellipse in Figure 14a). This makes it difficult to distinguish and identify the main arrivals without the real recording of the event for reference. Furthermore, the correlation coefficient is low at 0.15. SRI seismograms constructed at this largest length scale are thus less accurate than those constructed over shorter backbone seismometer-target sensor distances.

As shown for correlation-correlation SRI it appears that it is better to use only the backbone seismometers that are necessary to construct the arrivals of interest (e.g., those within the region in which the phase of the integrand of SRI integrals is approximately stationary [Snieder *et al.*, 2006b]) rather than including all possible backbone sensors. In the latter case one would hope that contributions to the SRI integrands from those backbone seismometers that do not construct arrivals of interest will cancel out to zero. We suspect that

correlation coefficients which have intermediate values of 0.57, 0.51, and 0.70, respectively. However, we note that there is a time shift in the reconstructions of these main arrivals compared to the real recordings.

Again, we propose that these inaccurate reconstructions are a consequence of the large backbone arrays used and thus an incorrect destructive/constructive interference of the data in equation (15). In Figure 14b we reconstruct the SRI seismograms at R29A, R30A, and R31A by invoking the criteria described above for an array restricted to backbone seismometers located within 250 km of the shortest backbone seismometer-target sensor distance. Thus, all backbone seismometers are located within 450 km of target sensors R29A, R30A, and R31A, in comparison to backbone seismometer-target sensor distances up to 1200 km in Figure 14a. For the reconstruction at target sensor R31A, we used seismometers along Lines 26A and 27A in this example as Line 28A is largely incomplete within the central region of the array that approximates the stationary-phase region (see Figure 13). Invoking the criteria for a restricted backbone array increases the correlation coefficients of the SRI seismograms as the main surface wave arrivals constructed by SRI are now in phase with the real earthquake recordings, and the time shifts observed in Figure 14a have been corrected.

At the largest length scale at target sensor GOGA, all backbone array seismometers along Lines 24A and 25A of the array shown in Figure 13a are used to construct the SRI seismogram in Figure 14a, as little increase in quality

such cancelation imposes more stringent requirements on the backbone array geometry than can generally be accommodated using real arrays.

5. Discussion

By using three separate example applications, we are able to assess the ability of source-receiver interferometry (SRI) to reconstruct seismograms on target seismometers across different spatial scales. On the two smaller length scales (up to ~ 540 km), the main surface wave arrivals of the SRI seismograms were in agreement with the real recordings, and some of the virtual reconstructions matched the recorded data some way into the coda (as found at a single length scale by *Curtis et al.* [2012]). However, at the largest length scale the SRI seismograms were poorly constructed as large spurious arrivals and significant time shifts were present in the virtual reconstructions compared to the real seismograms. These inaccurate reconstructions were a consequence of using all available backbone array seismometers, which led to incorrect constructive/destructive interference of the data in SRI integrals. We instead found that using spatially restricted backbone arrays that were scaled by the minimum backbone seismometer-target sensor distance constructed more reliable SRI seismograms.

5.1. Comparison of Correlation-Correlation SRI and Correlation-Convolution SRI

At the intermediate length scale we were able to compare directly the SRI seismograms constructed using two correlation integrals within SRI (Figure 8a, top four traces) to those seismograms constructed using the joint correlation-convolution approach (Figure 10). In the correlation-correlation reconstructions we identify spurious events that appear prior to the first surface wave arrivals (see the grey-shaded ellipse in Figure 8a). These spurious arrivals are associated with nonphysical energy that should cancel in the integration but does not when the medium is strongly scattering or when the surrounding source (or receiver) boundary is incomplete. Such nonphysical arrivals are constructed by cross correlating direct wavefields with scattered wavefields [*Halliday and Curtis*, 2009]. Under ideal conditions these nonphysical arrivals mutually cancel with nonphysical arrivals constructed by the cross correlation of purely scattered wavefields. However, when the medium is strongly attenuating, energy is lost during the propagation of the wavefields from the boundary sources (in this case noise sources) to the receiver locations. This introduces amplitude imbalances into the nonphysical arrivals, and they no longer mutually cancel, introducing artifacts into the interferometric estimations. Furthermore, *Halliday and Curtis* [2009] find that nonphysical arrivals are also enhanced when the source aperture is limited, i.e., when sources are not present at all required stationary-phase points. The same argument can also be made for a limited receiver aperture in inter-source interferometry, i.e., when spatial irregularities in the backbone array result in unoccupied stationary-phase points on the receiver boundary.

Since correlation refers to processes of complex conjugation (time-reversal), and wavefields cannot theoretically be time reversed in an attenuative medium without the reinjection of all of the lost (attenuated) energy, *Halliday and Curtis* [2009] propose that the method of convolution may be performed over correlation when attenuation is strong. When following a convolution approach, all nonphysical arrivals cancel to zero [*Halliday and Curtis*, 2009], and no artifacts are introduced into the interferometric result due to amplitude imbalances. Similarly, limited apertures do not introduce non-physical arrivals when using a convolution approach. We conclude that when the target sensors are located at intermediate distances from the backbone seismometer array (here, up to 540 km), and when the backbone seismometer geometry allows, correlation-convolution SRI is advantageous as the SRI propagators are constructed well via processes of correlation, and any nonphysical arrivals that do exist are suppressed in the inter-source interferometry step by processes of convolution.

5.2. Observing the Effect of Spatial Irregularities Within the Backbone Arrays

To compensate for spatial irregularities within the backbone arrays, and to thus discretize the inter-source interferometric integrals in equations (12) and (13) more precisely, the backbone seismometer arrays used in sections 4.3 and 4.4 were embedded within 2-D spatial Voronoi cells, the area of which provide $\Delta\mathbf{x}_i$ in equations (14) and (15). Figure 8b shows the SRI seismograms of the M 5.8 Mexico earthquake studied in section 4.3 constructed *without* Voronoi interpolation of the summand in equation (14). Instead, a simple summation was performed over the original (unweighted) values of the summand (i.e., without term $\Delta\mathbf{x}_i$) for each backbone seismometer. Comparing Figure 8b with Figure 8a, we observe that all matches between the real recordings and the SRI reconstructions are of a much poorer quality when the integration is performed

without Voronoi interpolation and include large-amplitude artifacts prior to the main surface waves. Since we use Voronoi interpolation to approximate the second step of SRI above, and since that step is simply the reciprocal of inter-receiver interferometry, it is likely that more generally Voronoi interpolation would increase the accuracy of most applications of interferometry where boundary source or receiver locations are known.

When reconstructing SRI seismograms at the intermediate length scale (section 4.3), only a small subset of the array seismometers were actually used in any one reconstruction, despite over 90 seismometers fitting the criteria outlined in section 4.1, and in both earthquake seismology examples (sections 4.3 and 4.4) only two lines of seismometers were used to create the SRI reconstructions. Surprisingly, preliminary studies on many data showed that a thicker band of seismometers did not improve the SRI results. This contradicts what might be expected given the results of *Draganov et al.* [2004], *Halliday and Curtis* [2008], and *Kimman and Trampert* [2010] whose work suggests that thicker boundaries should provide better results if the boundary is not in the very far field. For a target sensor located within or close to the backbone array, the final geometrical criteria that were highlighted by the preliminary studies and found to work best are described in section 4.1 and illustrated schematically in Figure 6.

We observed that even a slight deviation from these criteria can result in significantly poorer SRI reconstructions. For example, consider the first criterion in section 4.1, that the backbone array should comprise two parallel lines of approximately regularly spaced seismometers. This condition aims to fulfil the requirement that the backbone array seismometers occupy the stationary-phase points of the receiver boundaries in equations (14) and (15) [*Halliday and Curtis*, 2009]. In the backbone array shown in Figure 7 we observe that lines V and 3 are the most spatially irregular, comprising far fewer seismometers than the other lines. Seismometers along lines V and 3 were used to reconstruct the SRI seismograms at target sensors Z27A and 627A, respectively, and in Figure 8a we observe that the SRI seismograms constructed at these target sensors exhibit the lowest correlation coefficients. We thus conclude that these poorer reconstructions are partly a consequence of spatial irregularities within the two parallel lines of backbone array seismometers. This breaks the condition that receivers are to be located around the stationary-phase points of the receiver boundary and consequentially introduces nonphysical arrivals into the interferometric reconstructions as described above. Nevertheless, a comparison of Figure 8a with Figure 8b shows that Voronoi interpolation does contribute to resolve the issue of spatial irregularity as data are effectively interpolated into areas of the receiver boundary where seismometers are missing. It may be that in future a more accurate (higher-order) method of interpolation within and across Voronoi cells may further diminish such issues.

5.3. Performing SRI at the Largest Length Scale

The large-scale source and receiver geometries outlined in section 4.4 were chosen specifically to challenge the method: the limitations of SRI were identified and new criteria were established to correct for inaccurate data. We demonstrated the importance of correctly approximating the stationary-phase region of the receiver boundary S in equation (12) (or equation (13)) by comparing SRI seismograms constructed using all available backbone seismometers to those constructed using spatially restricted backbone arrays. For a given target sensor the restricted array consisted of seismometers located within 250 km of the shortest backbone seismometer-target sensor distance. Invoking this criteria for restricted arrays constructed SRI seismograms that were a significant improvement on SRI seismograms constructed using all available backbone seismometers (see Figures 12a, 12b, 14a, and 14b for comparisons of SRI seismograms).

We note, however, that at the largest length scale presented here at target sensor GOGA, the SRI seismogram of the M 6.5 earthquake was constructed poorly. We propose that this is a consequence of poorly constructed SRI propagators that are thus unable to redatum the earthquake energy from the backbone array seismometers to the locations of the most distant target sensors (e.g., due to a breakdown in the underlying assumption of zero attenuation for correlational interferometry).

5.4. The Role of the SRI Propagators

The inter-receiver Green's function estimates (the SRI propagators) are clearly key in SRI. They were constructed using noise interferometry in equation (9) and were selected to have a high signal-to-noise ratio (SNR) and hence (by our definition of SNR) are usually dominated by a main surface wave arrival. During the second correlational step of SRI, the phase of the propagators is subtracted from the phase of the backbone recordings through processes of time reversal. This has the effect of (computationally) redatuming

the recorded energy onto the target sensor location, but dominantly, this focuses the main surface wave arrival since that energy dominates the SRI propagators. To get the one-sided Green's function $G(\mathbf{x}, \mathbf{r})$ for this redatuming step in equations (14) and (15), the Green's function constructed at negative time in G_H was time reversed and added to the Green's function constructed at positive time. Since the results of noise interferometry are dependent on the directivity of the ambient wavefield, this would not be necessary if one side of the estimated Green's function was predominantly noise; instead, one could simply take the side within which the signal is constructed. Here we did not notice any particular consistent increase or decrease in the quality (signal-to-noise ratio) of the estimated Green's function when using a stacked summation of both sides of the Green's function, so we decided to continue with that approach to be consistent with previous studies.

Since attenuation may be an issue over long inter-receiver distances (e.g., from the backbone array to target sensor GOGA), another approach to estimate these propagators might be to use deconvolutional interferometry in place of correlational interferometry [Snieder and Safak, 2006]. The use of multidimensional deconvolution [Wapenaar *et al.*, 2008] has been shown to be able to compensate for various deficiencies in correlational interferometry, so there may be merit in future testing of deconvolutional forms of SRI.

5.5. Future Applications of SRI

In this study, target sensor WDC was located less than 200 km from the epicenter of the M 6.5 earthquake that occurred off the coast of California. Thus, it approaches the proximity of the location of rapid response local temporary seismometer arrays that are often deployed around large earthquake epicenters after the event has occurred, in order to continuously monitor the area for subsequent aftershocks. If such temporary seismometers are deployed for 6 months and ambient noise data are collected, this example shows that SRI might then be applied to construct local virtual seismograms of the earthquake retrospectively, even when the event occurs far away from the permanent backbone array. These virtual earthquake seismograms could then also be compared with any subsequent aftershocks recorded on the temporary seismometer array during its deployment. Alternatively, one can construct virtual SRI seismograms of an earthquake in almost real time using seismometers that used to be deployed close to where an earthquake has occurred, but which have since been removed. All that one requires is a backbone array of seismometers whose deployment spans both the time at which the earthquake occurred and the time during which the target sensors were previously deployed. In addition, the C3 (correlation of coda of correlation) method described by Ma and Beroza [2012] allows for the retrieval of Green's functions between pairs of seismometers whose times of deployment *do not* coincide. SRI propagators constructed from ambient noise observations recorded asynchronously could significantly increase the number of practical applications of SRI as all target sensor-backbone seismometer pairs would not need to be deployed coincidentally in time.

Furthermore, we see the benefit of seismometer arrays with deployment strategies similar to the USArray Transportable Array which routinely deploys approximately regularly spaced seismometers for up to 2 years before they are moved to a set of new locations. During their deployment, recordings of ambient seismic noise can be made on all seismometers and cross correlated to construct all possible inter-receiver Green's functions. This creates an archive of the propagators needed for SRI which can subsequently be inserted into equation (14) or equation (15) when an earthquake occurs. Virtual earthquake seismograms can then be reconstructed on any seismometer deployed before, during or after the event, provided that a suitably dense geometry of other seismometers recorded the earthquake. We note though that the ideal array deployment strategy for SRI would be for a dense backbone array to remain permanently in place while other roving sensors occupy temporary recording locations, as outlined in Curtis *et al.* [2012], which unfortunately was not the design of the deployment strategy used for USArray.

Finally, we comment on the results of Curtis *et al.* [2012] in which the SRI reconstructions were used to determine independent information about the source phase. In order to obtain this information correctly one would require the source-receiver geometry outlined in Figure 2a in which backbone seismometers occupy *both* stationary-phase regions of the boundary S surrounding the earthquake source at \mathbf{s} and the target sensor at \mathbf{r} (see the grey-shaded regions in Figure 2a for a schematic representation of these stationary-phase regions). Using both stationary-phase regions of the receiver boundary, one would correctly construct both the causal ($C = T^*G$) and acausal ($A = T^*G^*$) sides of $T^*G_H(\mathbf{r}, \mathbf{s})$ in equation (14). Curtis *et al.* [2012] then theoretically show that by calculating the ratio C/A , the phase of the source time function can be estimated independently from the phase of the Green's function, without using inverse theory. Such

independent phase information can then be used to obtain surface wave phase velocity estimates along event-to-seismometer paths that are an improvement on the estimates obtained from real recorded data alone. This application of SRI could thus improve the results of surface wave tomography studies. Unfortunately in the current study, we did not have backbone array seismometers in both stationary-phase regions; hence, we could not test this method here.

6. Conclusion

We demonstrate the construction of band-limited virtual seismograms of waves from seismic sources on sensors that were not necessarily deployed when the source occurred. We do this using both correlation-correlation and correlation-convolution source-receiver interferometry (SRI): cross correlations of seismic energy recorded over one period of time are used as propagators to redatum the source signals currently recorded at one set of locations onto new sensor locations, at any time after the source has occurred, using processes of correlation or convolution. The source signals need never be physically recorded at the new sensor locations.

This is possible on a variety of length scales and in a variety of settings. A small length scale, industrial seismics example uses correlation-correlation SRI to yield band-limited reconstructions of an active seismic shot on six sensors located up to 62 m from a regular line of receivers. An intermediate length scale example in an earthquake seismology setting uses correlation-correlation SRI to reconstruct virtual seismograms of a M 5.8 earthquake on eight target sensors located approximately between 210 km and 540 km from a backbone array of seismometers. Correlation-convolution SRI is also applied and is found to stabilize the SRI reconstructions, allowing spurious events to be identified that are associated with terms in equations that should (but may not) mutually cancel when using correlation-correlation SRI. The virtual earthquake seismograms constructed using SRI were compared with the real-event recordings and the quality of this match, as quantified by the correlation coefficient, was as high as 0.93 on one occasion. Finally, a large length scale example within an earthquake seismology setting was designed to challenge the methodology: this showed the limitations of correlation-correlation SRI and correlation-convolution SRI as virtual seismograms of a M 6.5 earthquake were reconstructed poorly (correlation coefficients as low as 0.15) on target sensors located up to 2420 km from a backbone array of seismometers. However, we showed that more robust SRI seismograms could be constructed by restricting the backbone array to include only those seismometers whose locations better approximated the stationary-phase points of the receiver boundary.

We show that discretizing the integrals from interferometric theory using Voronoi cell-based interpolation between seismometers on integral boundaries improves interferometric results significantly. We also constructed two completely new virtual seismograms. These are reconstructions of the earthquake seismograms on two sensors that were not deployed when the events occurred. When plotted alongside the virtual seismograms reconstructed on the target sensors at which we have real recordings for comparison, we see that all reconstructions follow the same moveout curves. All virtual earthquake seismograms were, however, constructed within a very narrow frequency band (0.04 Hz to 0.06 Hz) which currently limits the implementation of the data in future crustal seismology studies.

These multilength scale applications of SRI in both engineering and earthquake seismology settings begin to pave the way for a new type of seismology: a form of “retrospective seismology” where virtual seismograms can potentially be constructed at new, desired locations—locations determined after the energy from the source has dissipated and where, with hindsight, one would have liked to have had sensors installed.

References

- Bakulin, A., and R. Calvert (2004), *Virtual Source: New Method for Imaging and 4D Below Complex Overburden*, pp. 2477–2480, Society of Exploration Geophysicists, SEG Technical Program Expanded Abstracts, Denver, Colo.
- Behura, J., and R. Snieder (2013), Virtual real source: Source signature estimation using seismic interferometry, *Geophysics*, 78(5), Q57–Q68, doi:10.1190/GEO2013-0069.1.
- Bensen, G. D., M. H. Ritzwoller, M. P. Barmin, A. L. Levshin, F. Lin, M. P. Moschetti, N. M. Shapiro, and Y. Yang (2007), Processing seismic ambient noise data to obtain reliable broad-band surface wave dispersion measurements, *Geophys. J. Int.*, 169(3), 1239–1260, doi:10.1111/j.1365-246X.2007.03374.x.
- Bensen, G. D., M. H. Ritzwoller, and N. M. Shapiro (2008), Broadband ambient noise surface wave tomography across the United States, *J. Geophys. Res.*, 113, B05306, doi:10.1029/2007JB005248.
- Campillo, M., and A. Paul (2003), Long-range correlations in the diffuse seismic coda, *Science*, 299, 547–549, doi:10.1126/science.1078551.
- Cassereau, D., and M. Fink (1993), Focusing with plane time-reversal mirrors—An efficient alternative to closed cavities, *J. Acoust. Soc. Am.*, 94(4), 2373–2386, doi:10.1121/1.407457.

Acknowledgments

Thanks are extended to the British Geological Survey for their support, and to Craig Duguid and Schlumberger Gould Research, UK, for providing the data used in section 3 of this study. We thank the facilities of IRIS Data Services, and specifically the IRIS Data Management Center, for access to waveforms, related metadata, and/or derived products, as used in sections 2 and 3 of this study. IRIS Data Services are funded through the Seismological Facilities for the Advancement of Geoscience and EarthScope (SAGE) Proposal of the National Science Foundation under cooperative agreement EAR-1261681. Data from the TA network were made freely available as part of the EarthScope USArray facility, operated by Incorporated Research Institutions for Seismology (IRIS) and supported by the National Science Foundation, under cooperative agreement EAR-1261681.

- Curtis, A. (2009), Source-receiver seismic interferometry: 79th Annual International Meeting, SEG, expanded abstracts, 3655–3659, doi:10.1190/1.3255626.
- Curtis, A., and D. Halliday (2010), Source-receiver wave field interferometry, *Phys. Rev. E*, *81*(4,2), 046601, doi:10.1103/PhysRevE.81.046601.
- Curtis, A., P. G. Gerstoft, H. Sato, R. Snieder, and K. Wapenaar (2006), Seismic interferometry; turning noise into signal, *Leading Edge (Tulsa, OK)*, *25*(9), 1082–1092, doi:10.1190/1.2349814.
- Curtis, A., H. Nicolson, D. Halliday, J. Trampert, and B. Baptie (2009), Virtual seismometers in the subsurface of the Earth from seismic interferometry, *Nat. Geosci.*, *2*(10), 700–704, doi:10.1038/NGEO615.
- Curtis, A., Y. Behr, E. Entwistle, E. Galetti, J. Townend, and S. Bannister (2012), The benefit of hindsight in observational science: Retrospective seismological observations, *Earth Planet. Sci. Lett.*, *345–348*, 212–220, doi:10.1016/j.epsl.2012.06.008.
- Denolle, M. A., E. M. Dunham, G. A. Prieto, and G. C. Beroza (2013), Ground motion prediction of realistic earthquake sources using the ambient seismic field, *J. Geophys. Res. Solid Earth*, *118*, 2102–2118, doi:10.1029/2012JB009603.
- Denolle, M. A., E. M. Dunham, G. A. Prieto, and G. C. Beroza (2014), Strong ground motion prediction using virtual earthquakes, *Science*, *343*(6169), 399–403, doi:10.1126/science.1245678.
- Derode, A., E. Larose, M. Campillo, and M. Fink (2003a), How to estimate the Green's function of a heterogeneous medium between two passive sensors? Application to acoustic waves, *Appl. Phys. Lett.*, *83*(15), 3054–3056, doi:10.1063/1.1617373.
- Derode, A., E. Larose, M. Tanter, J. de Rosny, A. Tourin, M. Campillo, and M. Fink (2003b), Recovering the Green's function from field-field correlations in an open scattering medium (L), *J. Acoust. Soc. Am.*, *113*(6), 2973–2976, doi:10.1121/1.1570436.
- Draganov, D., K. Wapenaar, and J. Thorbecke (2004), Passive imaging in the presence of white noise sources, *The Leading Edge*, *9*, 889–892.
- Draganov, D., X. Campman, J. Thorbecke, A. Verdel, and K. Wapenaar (2013), Seismic exploration-scale velocities and structure from ambient seismic noise (> 1 Hz), *J. Geophys. Res. Solid Earth*, *118*, 4345–4360, doi:10.1002/jgrb.50339.
- Duguid, C., D. Halliday, and A. Curtis (2011), Source-receiver interferometry for seismic wavefield construction and ground-roll removal, *The Leading Edge*, *30*(8), 838–843, doi:10.1190/1.3626489.
- Galetti, E., and A. Curtis (2012), Generalised receiver functions and seismic interferometry, *Tectonophysics*, *532*, 1–26, doi:10.1016/j.tecto.2011.12.004.
- Halliday, D., and A. Curtis (2008), Seismic interferometry, surface waves and source distribution, *Geophys. J. Int.*, *175*(3), 1067–1087, doi:10.1111/j.1365-246X.2008.03918.x.
- Halliday, D., and A. Curtis (2009), Seismic interferometry of scattered surface waves in attenuative media, *Geophys. J. Int.*, *178*(1), 419–446, doi:10.1111/j.1365-246X.2009.04153.x.
- Halliday, D., and A. Curtis (2010), An interferometric theory of source-receiver scattering and imaging, *Geophysics*, *75*(6), SA95–SA103, doi:10.1190/1.3486453.
- Halliday, D., A. Curtis, and K. Wapenaar (2012), Generalized PP plus PS=SS from seismic interferometry, *Geophys. J. Int.*, *189*(2), 1015–1024, doi:10.1111/j.1365-246X.2012.05396.x.
- Halliday, D. F., A. Curtis, J. O. A. Robertsson, and D.-J. van Manen (2007), Interferometric surface-wave isolation and removal, *Geophysics*, *72*(5), A69–A73, doi:10.1190/1.2761967.
- Halliday, D. F., A. Curtis, P. Vermeer, C. Strobbia, A. Glushchenko, D. van Manen, and J. O. A. Robertsson (2010), Interferometric ground-roll removal: Attenuation of scattered surface waves in single-sensor data, *Geophysics*, *75*(2), SA15–SA25, doi:10.1190/1.3360948.
- Hong, T.-K., and W. Menke (2006), Tomographic investigation of the wear along the San Jacinto Fault, Southern California, *Phys. Earth Planet. Inter.*, *155*(3–4), 236–248, doi:10.1016/j.pepi.2005.12.005.
- Kedar, S. (2011), Source distribution of ocean microseisms and implications for time-dependent noise tomography, *C. R. Geosci.*, *343*(8–9), 548–557, doi:10.1016/j.crte.2011.04.005.
- Kimman, W. P., and J. Trampert (2010), Approximations in seismic interferometry and their effects on surface waves, *Geophys. J. Int.*, *182*(1), 461–476, doi:10.1111/j.1365-246X.2010.04632.x.
- King, S., and A. Curtis (2012), Suppressing nonphysical reflections in Green's function estimates using source-receiver interferometry, *Geophysics*, *77*(1), Q15–Q25, doi:10.1190/GEO2011-0300.1.
- Lobkis, O., and R. Weaver (2001), On the emergence of the Green's function in the correlations of a diffuse field, *J. Acoust. Soc. Am.*, *110*, 3011–3017, doi:10.1121/1.1417528.
- Löer, K., G. A. Meles, A. Curtis, and I. Vasconcelos (2014a), Diffracted and pseudo-physical waves from spatially limited arrays using source-receiver interferometry (SRI), *Geophys. J. Int.*, *196*(2), 1043–1059, doi:10.1093/gji/ggt435.
- Löer, K., G. Meles, and A. Curtis (2014b), Automatic identification of multiply diffracted waves and their ordered scattering paths, *J. Acoust. Soc. Am.*, in press.
- Ma, S., and G. C. Beroza (2012), Ambient-field Green's functions from asynchronous seismic observations, *Geophys. Res. Lett.*, *39*, L06301, doi:10.1029/2011GL050755.
- Meles, G. A., and A. Curtis (2014a), Discriminating physical and non-physical diffracted energy in source-receiver interferometry, *Geophys. J. Int.*, *197*(3), 1642–1659, doi:10.1093/gji/ggu054.
- Meles, G. A., and A. Curtis (2014b), Fingerprinting ordered diffractions in multiply diffracted waves, *Geophys. J. Int.*, *198*(3), 1701–1713, doi:10.1093/gji/ggu195.
- Nicolson, H., A. Curtis, B. Baptie, and E. Galetti (2012), Seismic interferometry and ambient noise tomography in the British Isles, *Proc. Geol. Assoc.*, *123*(1), 74–86, doi:10.1016/j.pgeola.2011.04.002.
- Nicolson, H., A. Curtis, and B. Baptie (2014), Rayleigh wave tomography of the British Isles from ambient seismic noise, *Geophys. J. Int.*, *198*, 637–655.
- Poliannikov, O. V. (2011), Retrieving reflections by source-receiver wavefield interferometry, *Geophysics*, *76*(1), SA1–SA8, doi:10.1190/1.3524241.
- Poliannikov, O. V., S. Rondenay, and L. Chen (2012), Interferometric imaging of the underside of a subducting crust, *Geophys. J. Int.*, *189*(1), 681–690, doi:10.1111/j.1365-246X.2012.05389.x.
- Ravasi, M., and A. Curtis (2013a), Nonlinear scattering based imaging in elastic media: Theory, theorems, and imaging conditions, *Geophysics*, *78*(3), S137–S155, doi:10.1190/GEO2012-0286.1.
- Ravasi, M., and A. Curtis (2013b), Elastic imaging with exact wavefield extrapolation for application to ocean-bottom 4C seismic data, *Geophysics*, *78*(6), S265–S284, doi:10.1190/GEO2013-0152.1.
- Ravasi, M., I. Vasconcelos, and A. Curtis (2014), Beyond conventional migration: Non-linear elastic subsalt imaging with transmissions and two-sided illumination, *Geophys. J. Int.*, *198*(2), 1173–1185, doi:10.1093/gji/ggu192.
- Rickett, J., and J. Claerbout (1999), Acoustic daylight imaging via spectral factorization: Helioseismology and reservoir monitoring, *The Leading Edge*, *18*(8), 957–960.

- Roux, P., and M. Fink (2003), Green's function estimation using secondary sources in a shallow water environment, *J. Acoust. Soc. Am.*, *113*(3), 1406–1416, doi:10.1121/1.1542645.
- Roux, P., K. Sabra, P. Gerstoft, W. Kuperman, and M. Fehler (2005), P-waves from cross-correlation of seismic noise, *Geophys. Res. Lett.*, *32*, L19303, doi:10.1029/2005GL023803.
- Sabra, K. G., P. Gerstoft, P. Roux, W. Kuperman, and M. Fehler (2005a), Extracting time-domain Green's function estimates from ambient seismic noise, *Geophys. Res. Lett.*, *32*, L03310, doi:10.1029/2004GL021862.
- Sabra, K. G., P. Gerstoft, P. Roux, W. A. Kuperman, and M. C. Fehler (2005b), Surface wave tomography from microseisms in Southern California, *Geophys. Res. Lett.*, *32*, L14311, doi:10.1029/2005GL023155.
- Sabra, K. G., S. Conti, P. Roux, and W. Kuperman (2007), Passive in vivo elastography from skeletal muscle noise, *Appl. Phys. Lett.*, *90*, 194101, doi:10.1063/1.2737358.
- Sambridge, M. (1999a), Geophysical inversion with a neighbourhood algorithm—I. Searching a parameter space, *Geophys. J. Int.*, *138*(2), 479–494, doi:10.1046/j.1365-246X.1999.00876.x.
- Sambridge, M. (1999b), Geophysical inversion with a neighbourhood algorithm—II. Appraising the ensemble, *Geophys. J. Int.*, *138*(3), 727–746, doi:10.1046/j.1365-246X.1999.00900.x.
- Sambridge, M., J. Braun, and H. McQueen (1995), Geophysical parametrization and interpolation of irregular data using natural neighbors, *Geophys. J. Int.*, *122*(3), 837–857, doi:10.1111/j.1365-246X.1995.tb06841.x.
- Schuster, G. (2001), Theory of daylight/interferometric imaging: Tutorial, EAGE, 63rd Conference and Technical Exhibition, Conference and Technical Exhibition, Extended Abstracts, A32.
- Schuster, G. (2009), *Seismic Interferometry*, Cambridge Univ. Press, New York.
- Schuster, G., J. Yu, J. Sheng, and J. Rickett (2004), Interferometric daylight seismic imaging, *Geophys. J. Int.*, *157*, 838–852, doi:10.1111/j.1365-246X.2004.02251.x.
- Shapiro, N. M., and M. Campillo (2004), Emergence of broadband Rayleigh waves from correlations of the ambient seismic noise, *Geophys. Res. Lett.*, *31*, L07614, doi:10.1029/2004GL019491.
- Shapiro, N. M., M. Campillo, L. Stehly, and M. H. Ritzwoller (2005), High-resolution surface-wave tomography from ambient seismic noise, *Science*, *307*(5715), 1615–1618, doi:10.1126/science.1108339.
- Shapiro, N. M., M. H. Ritzwoller, and G. D. Bensen (2006), Source location of the 26 sec microseism from cross-correlations of ambient seismic noise, *Geophys. Res. Lett.*, *33*, L18310, doi:10.1029/2006GL027010.
- Slob, E., and K. Wapenaar (2007), Electromagnetic Green's functions retrieval by cross-correlation and cross-convolution in media with losses, *Geophys. Res. Lett.*, *34*, L05307, doi:10.1029/2006GL029097.
- Slob, E., D. Draganov, and K. Wapenaar (2007), Interferometric electromagnetic Green's functions representations using propagation invariants, *Geophys. J. Int.*, *169*(1), 60–80, doi:10.1111/j.1365-246X.2006.03296.x.
- Sniieder, R. (2004), Extracting the Green's function from the correlation of coda waves: A derivation based on stationary phase, *Phys. Rev. E*, *69*(4,2), 046610, doi:10.1103/PhysRevE.69.046610.
- Sniieder, R., and E. Safak (2006), Extracting the building response using seismic interferometry: Theory and application to the Millikan Library in Pasadena, California, *Bull. Seismol. Soc. Am.*, *96*(2), 586–598, doi:10.1785/0120050109.
- Sniieder, R., J. Sheiman, and R. Calvert (2006a), Equivalence of the virtual-source method and wave-field deconvolution in seismic interferometry, *Phys. Rev. E*, *73*(6,2), 066620, doi:10.1103/PhysRevE.73.066620.
- Sniieder, R., K. Wapenaar, and K. Larner (2006b), Spurious multiples in seismic interferometry of primaries, *Geophysics*, *71*(4,5), S111–S1124, doi:10.1190/1.2211507.
- Sniieder, R., M. Miyazawa, E. Slob, I. Vasconcelos, and K. Wapenaar (2009), A comparison of strategies for seismic interferometry, *Surv. Geophys.*, *30*(4–5), 503–523, doi:10.1007/s10712-009-9069-z.
- Stehly, L., M. Campillo, and N. M. Shapiro (2007), Traveltime measurements from noise correlation: Stability and detection of instrumental time-shifts, *Geophys. J. Int.*, *171*(1), 223–230, doi:10.1111/j.1365-246X.2007.03492.x.
- Stehly, L., M. Campillo, B. Froment, and R. Weaver (2008), Reconstructing Green's function by correlation of the coda of the correlation (C^2) of ambient seismic noise, *J. Geophys. Res.*, *113*, B11306, doi:10.1029/2008JB005693.
- Tonegawa, T., and K. Nishida (2010), Inter-source body wave propagations derived from seismic interferometry, *Geophys. J. Int.*, *183*(2), 861–868, doi:10.1111/j.1365-246X.2010.04753.x.
- van Manen, D.-J., J. Robertsson, and A. Curtis (2005), Modeling of wave propagation in inhomogeneous media, *Phys. Rev. Lett.*, *94*(16), 164301, doi:10.1103/PhysRevLett.94.164301.
- van Manen, D.-J., A. Curtis, and J. Robertsson (2006), Interferometric modeling of wave propagation in inhomogeneous elastic media using time reversal and reciprocity, *Geophysics*, *71*(4,5), S147–S160, doi:10.1190/1.2213218.
- Vasconcelos, I. (2013), Source-receiver, reverse-time imaging of dual-source, vector-acoustic seismic data, *Geophysics*, *78*(2), WA123–WA145, doi:10.1190/GEO2012-0300.1.
- Vasconcelos, I., and J. Rickett (2013), Broadband extended images by joint inversion of multiple blended wavefields, *Geophysics*, *78*(2), WA147–WA158, doi:10.1190/GEO2012-0475.1.
- Vasconcelos, I., and R. Sniieder (2008a), Interferometry by deconvolution: Part 1—Theory for acoustic waves and numerical examples, *Geophysics*, *73*(3), S115–S128, doi:10.1190/1.2904554.
- Vasconcelos, I., and R. Sniieder (2008b), Interferometry by deconvolution: Part 2—Theory for elastic waves and application to drill-bit seismic imaging, *Geophysics*, *73*(3), S129–S141, doi:10.1190/1.2904985.
- Vasconcelos, I., P. Sava, and H. Douma (2010), Nonlinear extended images via image-domain interferometry, *Geophysics*, *75*(6), SA105–SA115, doi:10.1190/1.3494083.
- Wang, B., P. Zhu, Y. Chen, F. Niu, and B. Wang (2008), Continuous subsurface velocity measurement with coda wave interferometry, *J. Geophys. Res.*, *113*, B12313, doi:10.1029/2007JB005023.
- Wapenaar, K. (2003), Synthesis of an inhomogeneous medium from its acoustic transmission response, *Geophysics*, *68*(5), 1756–1759, doi:10.1190/1.1620649.
- Wapenaar, K. (2004), Retrieving the elastodynamic Green's function of an arbitrary inhomogeneous medium by cross correlation, *Phys. Rev. Lett.*, *93*(25), 254301, doi:10.1103/PhysRevLett.93.254301.
- Wapenaar, K., and J. Fokkema (2006), Green's function representations for seismic interferometry, *Geophysics*, *71*, S133–S146, doi:10.1190/1.2213955.
- Wapenaar, K., J. van der Neut, and E. Ruigrok (2008), Passive seismic interferometry by multidimensional deconvolution, *Geophysics*, *73*(6), A51–A56, doi:10.1190/1.2976118.
- Wapenaar, K., D. Draganov, R. Sniieder, X. Campman, and A. Verdel (2010a), Tutorial on seismic interferometry: Part 1—Basic principles and applications, *Geophysics*, *75*(5), A195–A209, doi:10.1190/1.3457445.

- Wapenaar, K., E. Slob, R. Snieder, and A. Curtis (2010b), Tutorial on seismic interferometry: Part 2—Underlying theory and new advances, *Geophysics*, 75(5), A211–A227, doi:10.1190/1.3463440.
- Wapenaar, K., J. van der Neut, E. Ruigrok, D. Draganov, J. Hunziker, E. Slob, J. Thorbecke, and R. Snieder (2011), Seismic interferometry by crosscorrelation and by multidimensional deconvolution: A systematic comparison, *Geophys. J. Int.*, 185(3), 1335–1364, doi:10.1111/j.1365-246X.2011.05007.x.
- Weaver, R., and O. Lobkis (2001), Ultrasonics without a source: Thermal fluctuation correlations at MHz frequencies, *Phys. Rev. Lett.*, 87, 134301, doi:10.1103/PhysRevLett.87.134301.
- Xiao, X., M. Zhou, and G. T. Schuster (2006), Salt-flank delineation by interferometric imaging of transmitted P- to S-waves, *Geophysics*, 71(4,S), S1197–S1207, doi:10.1190/1.2209550.
- Yang, Y., and M. H. Ritzwoller (2008), Characteristics of ambient seismic noise as a source for surface wave tomography, *Geochem. Geophys. Geosyst.*, 9, Q02008, doi:10.1029/2007GC001814.
- Zeng, X., and S. Ni (2014), Evidence for an independent 26-s microseismic source near the Vanuatu Islands, *Pure Appl. Geophys.*, 171(9), 2155–2163, doi:10.1007/s00024-014-0811-1.